Higher-Order Topological Band Structures

Trifunovic, Luka ; Brouwer, Piet W

Abstract: The interplay of topology and symmetry in a material's band structure may result in various patterns of topological states of different dimensionality on the boundary of a crystal. The protection of these "higher-order" boundary states comes from topology, with constraints imposed by symmetry. Herein, the bulk–boundary correspondence of topological crystalline band structures, which relates the topology of the bulk band structure to the pattern of the boundary states, is reviewed. Furthermore, recent advances in the K-theoretic classification of topological crystalline band structures are discussed.

DOI: https://doi.org/10.1002/pssb.202000090

physica status solidi pss b
www.pss-b.com

Higher-Order Topological Band Structures

Luka Trifunovic and Piet W. Brouwer*

The interplay of topology and symmetry in a material's band structure may result in various patterns of topological states of different dimensionality on the boundary of a crystal. The protection of these "higher-order" boundary states comes from topology, with constraints imposed by symmetry. Herein, the bulk–boundary correspondence of topological crystalline band structures, which relates the topology of the bulk band structure to the pattern of the boundary states, is reviewed. Furthermore, recent advances in the *K*-theoretic classification of topological crystalline band structures are discussed.

1. Introduction

Traditionally, the understanding of a material's band structure requires knowledge of symmetry representation theory. During the last decades, it became increasingly clear that not only symmetries, but also concepts borrowed from topology, and often a combination of the two, are required for a complete understanding of band structures.[1–4] In particular, gapped band structures can be classified into different topological classes (also referred to as "topological phases"), where two band structures are in the same class if they can be smoothly deformed into each other by changing system parameters, without closing the excitation gap and without reducing the symmetry of the band structure at an intermediate stage. This topological classification of band structures applies equally well to superconductors if these have a gapped excitation spectrum in their Bardeen–Cooper–Schrieffer (BCS) mean-field description.

An important practical consequence of the existence of distinct topological classes of band structures is that a nontrivial topology of the bulk band structure may imply the existence of anomalous boundary states. A boundary state is called "anomalous" if it cannot exist without the presence of the topological bulk. Anomalous boundary states are immune to local perturbations and can be removed only by a perturbation that closes the excitation gap of the bulk band structure or reduces its symmetry. This connection between a nontrivial topology of the bulk band structure and the existence of anomalous boundary states is referred to as *bulk–boundary correspondence*. For topological phases that are subject to nonspatial symmetries only, such as time-reversal symmetry or the particle–hole antisymmetry of the superconducting Bogoliubov–de Gennes Hamiltonian, the bulk–boundary correspondence is complete: Each topological class of a d-dimensional bulk band structure is uniquely associated with an anomalous boundary state of dimension $d-1$ and vice versa.[5,6]

The question of a bulk–boundary correspondence for topological phases that are also subject to spatial symmetries, such as inversion or mirror symmetries, is more subtle. In general, in this case the bulk–boundary correspondence is incomplete and requires a degree of compatibility of the crystal termination and the crystalline symmetries. Immediately after the discovery of topological crystalline band structures,[7,8] it was understood that a conventional bulk–boundary correspondence, in which the anomalous boundary states of a d-dimensional crystal have dimension $d-1$, exists only for a boundary orientation that is invariant under the action of the crystalline symmetry group.[2,7–12] This condition, however, can be met for a small number of symmetry groups only—mirror symmetry being an example—and even in those cases is restricted to selected surface orientations. Recently, following pioneering work by Schindler et al.,[13] it was realized that topological crystalline phases may also have anomalous boundary signatures of dimension less than $d-1$,[13–26] provided the crystal termination as a whole respects the crystalline symmetry group. Examples are anomalous states at hinges or corners of a 3D crystal or anomalous corner states of a 2D crystal (see **Figure 1**). The condition that the crystal termination as a whole respects the crystalline symmetry group is a much weaker condition on the surface orientations than the condition that the orientation of individual crystal faces is invariant under the crystalline symmetry. Moreover, it is a condition that can be met for all crystalline symmetry groups. Topological phases with this type of boundary signature are called *higher-order* topological phases, where the order n indicates the *codimension* of the boundary states. In this terminology, topological phases that do not rely on crystalline symmetries, which have boundary states of dimension $d-1$, are called "first-order."

Boundary states of codimension $n \geq 2$ may also occur as the anomalous boundary states of a nontrivial topological phase located on the crystal boundary.[15,27–29] As such states do not

Dr. L. Trifunovic
Department of Physics
University of Zurich
Winterthurerstrasse 190, 8057 Zurich, Switzerland
E-mail: luka.trifunovic@uzh.ch

Prof. P. W. Brouwer
Dahlem Center for Complex Quantum Systems and Physics Department
Freie Universität Berlin
Arnimallee 14, 14195 Berlin, Germany

The ORCID identification number(s) for the author(s) of this article can be found under https://doi.org/10.1002/pssb.202000090.

DOI: 10.1002/pssb.202000090

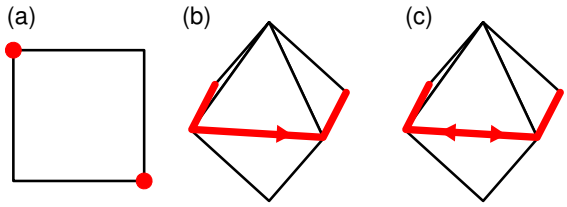

Figure 1. Examples of higher-order boundary signatures: a) Majorana corner states of a 2D topological crystalline superconductor, b) chiral hinge states of a 3D second-order Chern insulator, and c) helical hinge states of a second-order topological insulator.

have their origin in the topology of the bulk band structure, they are referred to as *extrinsic*;[18] anomalous boundary states that are rooted in the topology of the bulk band structure are called *intrinsic*. Although they are a property of the crystal termination, extrinsic anomalous boundary states still have some degree of topological protection. Specifically, extrinsic corner states cannot be removed by perturbations that respect the crystalline symmetries and do not close the gaps along hinges or surfaces of the crystal. Similarly, extrinsic hinge states cannot be removed by symmetry-preserving perturbations that do not close surface gaps.

In this article, we review the arguments that show how intrinsic higher-order boundary states arise as a consequence of a topologically nontrivial band structure. We discuss the simplified model systems that appeared in the original publications and that have become paradigmatic examples of higher-order topological band structures. We also discuss the bulk–boundary correspondence for topological crystalline phases. Such bulk–boundary correspondence was formulated by us for the case of "order-two" crystalline symmetries that square to the identity, such as mirror, inversion, or twofold rotation in Trifunovic and Brouwer.[21] Here, these ideas are extended to more general crystalline symmetry groups. Throughout the review, we restrict ourselves to "strong" topological phases, which are robust to a breaking of the lattice translation symmetry (while preserving the crystalline symmetries, of course).

We note that the relevance of topology to condensed matter systems is not only limited to understanding band structures. Indeed, as the pioneering work of Thouless et al. shows,[30] the topological classes for quantized Hall systems can be defined even in the absence of a discrete translation symmetry. The results for strong topological phases that we consider in this review, such as the bulk–boundary correspondence in presence of a crystalline symmetry, remain valid if the lattice translation symmetry is broken in a manner that preserves the crystalline symmetries. Some auxiliary results, such as the definition of topological invariants, rely on the existence of a band structure.

The remainder of this article is organized as follows: In Section 2, we briefly review the ground rules for defining topological equivalence. In Section 3, we discuss three paradigmatic examples of topological band structures in one, two, and three dimensions, their boundary signatures, and how and under what conditions the existence of these boundary signatures is rooted in the topology of the bulk band structure. In addition, we review recent experimental realizations of higher-order topology. In Section 4, we formulate the formal bulk–boundary correspondence for topological band structures with a crystalline symmetry. In Section 5, we discuss a specific example to make the rather general considerations of Section 4 more explicit. We conclude in Section 6.

2. Topological Equivalence

For a precise topological classification of band structures and the associated boundary signatures, one has to define the "rules" of topological equivalence. When taken literally, the definition of topological equivalence stated in the first paragraph of the introduction implies that two band structures with different numbers of occupied bands belong to different classes. It is customary to relax this criterion and allow that the separate addition of (topologically trivial) occupied or empty bands or sets of bands does not change the topological class of the band structure. This topological equivalence of band structures modulo the addition of trivial occupied or empty bands is known as "stable equivalence." The complete bulk-boundary correspondence for topological band structures subject to non-spatial symmetries was derived using the rules of stable equivalence.[5,6]

More precisely, under the rules of stable equivalence one considers pairs (H, H') of band structures with an equal number of bands—an approach known as the *Grothendieck construction*. Two pairs (H_1, H'_1) and (H_2, H'_2) are considered topologically equivalent if $H_1 \bigoplus H'_2$ can be smoothly deformed into $H_2 \bigoplus H'_1$, without closing the excitation gap and without violating the symmetry constraints. With this definition, topological classes acquire a group structure, the group operation being the direct sum of band structures: Using the pair (H, H') to represent its topological class, the group operation is $(H_1, H'_1) \bigoplus (H_2, H'_2) = (H_1 \bigoplus H_2, H'_1 \bigoplus H'_2)$. The inverse group operation is also defined: $(H_1, H'_1) \ominus (H_2, H'_2) = (H_1 \bigoplus H'_2, H_2 \bigoplus H'_1)$. In this manner, the topological phases are classified with an Abelian *classifying group K*. The corresponding classification scheme is known as the "*K*-theory classification".

3. Boundary Signatures of Topological Band Structures

In this section, we first consider three examples of gapped band structures with crystalline symmetries in dimensions $d = 1$, 2, and 3. The examples are meant to illustrate the role of the crystalline symmetries as well as the nonspatial symmetries for the topological characterization of the band structure and the protection of eventual boundary states. Subsequently, we review recent experiments that realize higher-order topological band strucutres. The last three subsections explain how and when the boundary signatures derive from the nontrivial topology of the bulk band structure.

3.1. 1D Model with Inversion Symmetry

As a first example, we consider the 1D model known as the Su–Schrieffer–Heeger model or the "Kitaev chain" in its non-superconducting or superconducting realizations, respectively[31,32]

$$H(k) = \Gamma_0[m + t(1 - \cos k)] + \Gamma_1 t \sin k \tag{1}$$

with "Dirac gamma matrices" $\Gamma_0 = \sigma_1$ and $\Gamma_1 = \sigma_2$. The model is invariant under particle–hole conjugation $\mathcal{P}$

$$H(k) = -U_{\mathcal{P}} H(-k)^* U_{\mathcal{P}} \tag{2}$$

with $U_{\mathcal{P}} = \sigma_3$. If $\mathcal{P}$ is not enforced, Equation (1) represents a 1D chain with a two-atom unit cell and nearest-neighbor hopping amplitudes that alternate between t and $t + m$ (see **Figure 2**a). With particle–hole symmetry, Equation (1) represents the Bogoliubov–de Gennes Hamiltonian of a 1D superconductor with a one-atom unit cell, be it with a nonstandard form of the particle–hole conjugation operation. In addition, the Hamiltonian (Equation (1)) is also invariant under time reversal $\mathcal{T}$, the "chiral antisymmetry" $U_{\mathcal{C}}$, and inversion $\mathcal{T}$

$$\begin{aligned} H(k) &= U_{\mathcal{T}} H(-k)^* U_{\mathcal{T}} \\ &= -U_{\mathcal{C}} H(k) U_{\mathcal{C}} \\ &= U_{\mathcal{I}} H(-k) U_{\mathcal{I}} \end{aligned} \tag{3}$$

with $U_{\mathcal{T}} = 1$, $U_{\mathcal{C}} = U_{\mathcal{P}} U_{\mathcal{T}} = 3$, and $U_{\mathcal{I}} = \Gamma_0 = \sigma_1$. The inversion operation $\mathcal{I}$ commutes with $\mathcal{T}$, but it anticommutes with $\mathcal{P}$, so this model represents an odd-parity superconductor if $\mathcal{P}$ is present.

The model (1) describes a one-parameter family of Hamiltonians $H(k)$, labeled by the parameter m. The spectral gap of the model (1) closes at $m = 0$. To see whether this gap closing point represents a topological phase transition, one looks for the existence of "mass terms," perturbations to $H(k)$ that anticommute with the matrices Γ_0 and Γ_1. If such mass terms do not exist, a gap closing can not be avoided when m is tuned through the gapless point at $m = 0$ and the gapless point represents a topological phase transition. If it exists, the phases below and above $m = 0$ are topologically equivalent.

By inspection, one easily verifies that the model (1) allows a single mass term, $M = \sigma_3$. This mass term is, however, incompatible with $\mathcal{P}$, $\mathcal{C}$, or $\mathcal{I}$, so the gapless point at $m = 0$ represents a topological phase transitions if at least one of these three symmetries is present. With $\mathcal{P}$ or $\mathcal{C}$, the model (1) is in a first-order (i.e., noncrystalline) topological phase for $-2t < m < 0$ with a (Majorana) zero mode at each end. Without $\mathcal{P}$ or $\mathcal{C}$, but with $\mathcal{I}$, the model no longer has protected zero-energy end states, but it has an anomalous half-integer "end charge" if $-2t < m < 0$. The existence of the end charge follows from a calculation of the bulk polarization.[33] It can also be inferred from the fact that the midgap end state in the presence of $\mathcal{P}$ or $\mathcal{C}$ symmetrically removes a half-integer charge from the valence and conduction bands. If $\mathcal{P}$ or $\mathcal{C}$ is broken, the end states can be removed, for example, by a local potential at each end, but the half-integer end charge is immune to the addition of a local perturbation, as the inversion symmetry $\mathcal{I}$ prevents charge flow through the insulating bulk. If $\mathcal{P}$, $\mathcal{C}$, and $\mathcal{I}$ are broken, the existence of the mass term $M = \sigma_3$ implies that the model is topologically trivial.

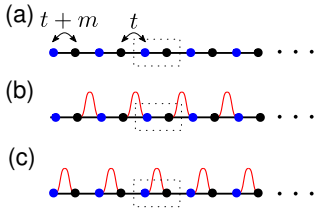

Figure 2. a) Without particle–hole symmetry, the model (1) describes a 1D lattice with a two-atom unit cell and nearest-neighbor hopping amplitudes that alternate between t and $t + m$. b) In the "topological phase" $-2t < m < 0$ Wannier functions are localized between unit cells, whereas c) they are localized in the center of the unit cells if $m < -2t$ or $m > 0$. The two patterns cannot be smoothly deformed into each other in the presence of inversion symmetry.

Having no anomalous end states, the model (1) with broken $\mathcal{P}$ or $\mathcal{C}$ symmetry is an example of a "Wannierizable" or "atomic limit" band structure, a band structure for which there exists a basis of localized "Wannier functions." That such atomic-limit band structures can nevertheless be topologically distinct can be seen by inspecting the model (1) in the limits $t/m = -1$ and $t/m = 0$ in which the system dimerizes and the eigenstates are trivially constructed. For $t/m = 0$, the Wannier states are localized in the center of the unit cells, whereas for $t/m = -1$ the Wannier states exist at the boundary of the unit cells (see Figure 2b,c). As it is not possible to continuously move Wannier states from the position in Figure 2b to the position in Figure 2c without breaking the inversion symmetry, the two cases represent different topological phases. As it is the presence of a crystalline symmetry that rules out a continuous transition between the two topological phases, such topologically different atomic-limit insulators are referred to as "symmetry-obstructed atomic insulators."[34,35]

One-dimensional gapped Hamiltonians with inversion symmetry, but without particle–hole antisymmetry, have a $\mathbb{Z}$ classification,[9–12,36] the topological index N corresponding to the difference of the number of occupied odd-parity bands at $k = \pi$ and $k = 0$. The generator of the classifying group is the topological equivalence class of the model (1) with $-2t < m < 0$. There are no anomalous corner charges, or any other boundary boundary signatures, if $\mathcal{N}$ is even.

3.2. BBH Model

The first model featuring intrinsic anomalous corner states was considered by Benalcazar, Bernevig, and Hughes (BBH).[14,37] It is a four-band model

$$\begin{aligned} H(k_1, k_2) = {} & \Gamma_+(t' + t\cos k_1) + \Gamma_1 t \sin k_1 \\ & + \Gamma_-(t' + t\cos k_2) + \Gamma_2 t \sin k_2 \end{aligned} \tag{4}$$

where t and t' are real parameters and $\Gamma_+ = \tau_1\sigma_0$, $\Gamma_- = -\tau_2\sigma_2$, $\Gamma_1 = -\tau_2\sigma_3$, $\Gamma_2 = -\tau_2\sigma_1$ are mutually anticommuting Hermitian matrices that square to one. The Hamiltonian (Equation (4)) satisfies two mirror symmetries $\mathcal{M}_{x,y}$

$$\begin{aligned} H(k_1, k_2) &= U_x H(-k_1, k_2) U_x \\ &= U_y H(k_1, -k_2) U_y \end{aligned} \tag{5}$$

with $U_x = \tau_1\sigma_3$ and $U_y = \tau_1\sigma_1$, as well as a fourfold rotation symmetry $\mathcal{R}_4$ with $(\mathcal{R}_4)^4 = -1$

$$H(k_1, k_2) = U_R H(k_2, -k_1) U_R^\dagger \tag{6}$$

with

$$U_R = \begin{pmatrix} 0 & \sigma_0 \\ -i\sigma_2 & 0 \end{pmatrix} \tag{7}$$

Like the previous example, the Hamiltonian (Equation (4)) is invariant under time reversal $\mathcal{T}$, particle–hole conjugation $\mathcal{P}$, and the chiral antisymmetry $\mathcal{C}$

$$\begin{aligned} H(k_1, k_2) &= U_\mathcal{T} H(-k_1, -k_2)^* U_\mathcal{T} \\ &= -U_\mathcal{P} H(-k_1, -k_2)^* U_\mathcal{P} \\ &= -U_\mathcal{C} H(k_1, k_2) U_\mathcal{C} \end{aligned} \tag{8}$$

with $U_\mathcal{T} = 1$, $U_\mathcal{P} = U_\mathcal{C} = \tau_3$. In the presence of particle–hole symmetry, the BBH model (4) may be understood as a superconductor with a two-atom unit cell. In this case, the order parameter has odd mirror parity, but it transforms trivially under rotations. Without $\mathcal{P}$, Equation (4) has an intuitive explanation in terms of a tight-binding model on the square lattice with a four-atom unit cell (see **Figure 3**).

Equation (4) does not have the Dirac-like form of Equation (1), which allows a straightforward analysis of its topological content by counting mass terms. However, it can be smoothly transformed to a Hamiltonian of that form. This is most conveniently performed in the vicinity of the gapless point at $t' = \pm t$ by parameterizing

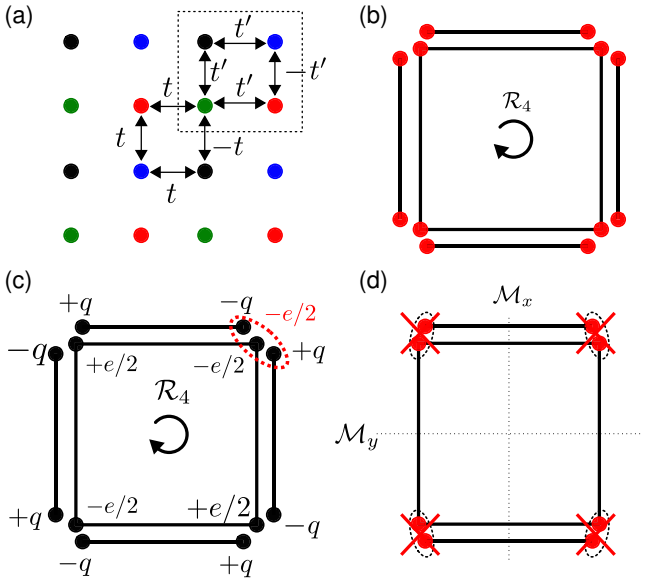

Figure 3. a) Representation of the BBH model as a lattice model with a four-atom unit-cell and nearest-neighbor hopping. With fourfold rotation symmetry $\mathcal{R}_4$ the model exhibits zero-energy corner states in the presence of $\mathcal{P}$ or $\mathcal{C}$. b) These corner states are intrinsic: They cannot be removed by an $\mathcal{R}_4$-compatible change of boundary termination. With $\mathcal{R}_4$, but without $\mathcal{P}$ and $\mathcal{C}$, the corners may have anomalous half-integer charges. c) These, too, cannot be removed by an $\mathcal{R}_4$-compatible change of boundary termination. d) If $\mathcal{R}_4$ is broken, zero-energy corner states can be removed by suitably added decorations, regardless of the presence of the mirror symmetries $\mathcal{M}_x$ and $\mathcal{M}_y$.

$$t' = -t + m/2 \tag{9}$$

and rewriting Equation (4) as

$$\begin{aligned} H(k_1, k_2) = \Gamma_0[m + t(2 - \cos k_1 - \cos k_2)] \\ + \Gamma_1 t \sin k_1 + \Gamma_2 t \sin k_2 \\ - \Gamma_4 t(\cos k_1 - \cos k_2) \end{aligned} \tag{10}$$

where $\Gamma_\pm = -(\Gamma_0 \pm \Gamma_4)/\sqrt{2}$ and we rescaled the terms proportional to $\Gamma_{0,4}$. In the vicinity of the gapless point $m = 0$, the term proportional to Γ_4 can be sent to zero without violating any of the symmetries or closing a spectral gap. The remaining three terms have the desired Dirac-like form (compare with Equation (1)).

Whether the gapless point at $m = 0$ represents a topological phase transition can be easily decided by inspection of the "mass terms" of the Hamiltonian (Equation (10)). There are two such mass terms: $M_1 = \Gamma_4$ and $M_2 = \tau_3\sigma_0$. The first of these is compatible with all symmetries discussed above, except for $\mathcal{R}_4$, which implies that the model (4) is topologically trivial unless $\mathcal{R}_4$ is present. The mass term M_2 is compatible with $\mathcal{T}$ and with twofold rotation symmetry $\mathcal{R}_2 = \mathcal{M}_x\mathcal{M}_y$ only.

With fourfold rotation symmetry, the model (4) has a nontrivial topological phase for $-4t < m < 0$. In the presence of $\mathcal{P}$ or $\mathcal{C}$, this phase has anomalous zero-energy (Majorana) corner states. If $\mathcal{P}$ or $\mathcal{C}$ are broken, the corner states may be removed by a local perturbation. In this case, the model (4) is in an obstructed atomic-limit phase in which—analogously to the 1D example discussed previously—anomalous half-integer corner charges remain.[14,37,38] These corner states or corner charges are *intrinsic*: They are a consequence of the topology of the bulk band structure and they exist independently of the lattice termination, as long as the termination is compatible with the fourfold rotation symmetry $\mathcal{R}_4$.[39] To see this, observe that the relevant changes of boundary termination correspond to "decorating" the boundaries with 1D chains with a gapped excitation spectrum. Although such "decorations" may have zero-energy (Majorana) end states (with $\mathcal{P}$ or $\mathcal{C}$) or fractional end charges (without $\mathcal{P}$ and $\mathcal{C}$), the requirement that the decoration be $\mathcal{R}_4$-compatible means that the net number of zero-energy states added to each corner is even (with $\mathcal{P}$ or $\mathcal{C}$) or that the net charge added to each corner is an integer (without $\mathcal{P}$ or $\mathcal{C}$)[38,40] (see Figure 3).

The bulk band structure of Equation (4) is always trivial if $\mathcal{R}_4$ is broken. Benalcazar et al.[14,37] show that the model (4) exhibits a phase with a quantized quadrupole moment in the presence of the two mirror symmetries $\mathcal{M}_x$ and $\mathcal{M}_y$. The quantized quadrupole moment is associated with the bulk band structure. Despite it being quantized for a generic gapped crystalline phase protected by $\mathcal{M}_x$ and $\mathcal{M}_y$, the quadrupole moment is, however, not a topological invariant, as it can change its value without a closing of the bulk excitation gap. Nevertheless, if $\mathcal{R}_4$ is broken, zero-energy corner states may also exist if $\mathcal{P}$ or $\mathcal{C}$ is present. In this case, the corner states are *extrinsic*: Their existence depends on the lattice termination and they may be removed by decorating the boundaries with 1D gapped chains (see Figure 3). The same applies to the existence of half-integer corner charges for the case that $\mathcal{P}$ and $\mathcal{C}$ are broken. The presence or absence of the two mirror symmetries $\mathcal{M}_{x,y}$ does not affect these conclusions.

Two-dimensional gapped Hamiltonians with intrinsic anomalous corner states realize a *second-order* topological phase. The example of the BBH model shows that the identification of the relevant nonspatial and crystalline symmetries is key to deciding whether or not a given band structure represents a second-order topological phase. Indeed, the very same model (4) with the same choice of parameters $-4t < m < 0$ may be a second-order phase, an obstructed atomic-limit phase, or a trivial phase depending on whether or not $\mathcal{P}$ or $\mathcal{C}$ and fourfold rotation symmetry $\mathcal{R}_4$ are enforced.

As in the 1D example discussed in Section 3.1, the BBH model is part of a larger family of topological Hamiltonians. For example, 2D Hamiltonians with $\mathcal{P}$ and $\mathcal{R}_4$ have a $\mathbb{Z}^3$ classification,[41–43] where one factor $\mathbb{Z}$ describes a first-order topological phase with chiral (Majorana) edge modes. The second factor $\mathbb{Z}$ describes a sequence of topological phases for which the topological class of the BBH model (4) with $-4t < m < 0$ is the generator. There are no anomalous corner states if the corresponding topological index is even, consistent with the $\mathbb{Z}_2$ nature of the Majorana corner modes. The last factor $\mathbb{Z}$ describes additional atomic-limit phases without boundary signatures.

3.3. 3D Example

As a third example, we discuss a 3D generalization of the BBH model originally proposed by Schindler et al.[13]

$$\begin{aligned} H(\vec{k}) = {} & \Gamma_0[m + t(3 - \cos k_1 - \cos k_2 - \cos k_3)] \\ & + \Gamma_1 t \sin k_1 + \Gamma_2 t \sin k_2 + \Gamma_3 t \sin k_3 \\ & + \Gamma_4 t'(\cos k_1 - \cos k_2) \end{aligned} \tag{11}$$

where $\Gamma_0 = \tau_3\sigma_0$, $\Gamma_k = \tau_1\sigma_k$, $k = 1, 2, 3$, and $\Gamma_4 = \tau_2\sigma_0$. As in the previous example (see Equation (10)), the last term proportional to Γ_4 may be omitted without closing the spectral gap or violating any of the symmetries. Without this last term, the model (11) is invariant under time-reversal $\mathcal{T}$

$$H(\vec{k}) = U_{\mathcal{T}} H(-\vec{k})^* U_{\mathcal{T}} \tag{12}$$

with $U_{\mathcal{T}} = \tau_0\sigma_2$, as well as a fourfold rotation $\mathcal{R}_4$

$$H(k_1, k_2, k_3) = U_{\mathcal{R}} H(k_2, -k_1, k_3) U_{\mathcal{R}}^{-1} \tag{13}$$

with $U_{\mathcal{R}} = \tau_0 e^{i\pi\sigma_3/4}$. The model (11) has a single mass term $M = \Gamma_4$, which is antisymmetric under $\mathcal{T}$ and symmetric under $\mathcal{R}_4$.

In the presence of $\mathcal{T}$ the gapless point $m = 0$ is a topological phase transition between phases with and without gapless surface states, irrespective of the fourfold rotation symmetry $\mathcal{R}_4$. Schindler et al. observed that the mass term $M = \Gamma_4$ is not only antisymmetric under $\mathcal{T}$, but also under the product $\mathcal{T}\mathcal{R}_4$, so if $\mathcal{T}\mathcal{R}_4$ is a good symmetry, the gapless point $m = 0$ still separates topologically different band structures, even if $\mathcal{T}$ and $\mathcal{R}_4$ symmetries are broken individually. In this case, the topological phase is not characterized by gapless surface states (because these are gapped out on a generic surface if time-reversal symmetry is broken), but by a chiral gapless mode running along the crystal "hinges" (see **Figure 4**). This gapless mode is a manifestation of the topological nature of the bulk band structure and it cannot be removed by changing the crystal termination. This can be understood by noting that the relevant change of surface termination corresponds to decorating each of the four crystal faces by a 2D quantized Hall insulator, which will change the number of chiral modes running along a hinge by an even number if the surface decoration is compatible with the $\mathcal{T}\mathcal{R}_4$ symmetry (see Figure 4b). A boundary pattern shown in Figure 4a, which has an odd number of chiral modes at each hinge, is "anomalous"—it cannot exist without a topologically nontrivial 3D bulk. Because of the existence of anomalous boundary states of codimension two, the model (11) is a *second-order* topological phase.

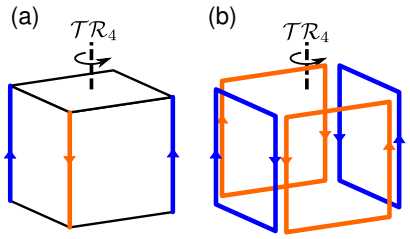

Figure 4. a) Configuration of chiral hinge modes of a 3D crystal with $\mathcal{T}\mathcal{R}_4$ symmetry. b) Configurations of chiral hinge modes that can be obtained by "decorating" the boundary have an even number of chiral modes at each hinge.

The same boundary phenomenology can exist in the absence of crystalline symmetries. An early example was proposed by Sitte et al., who showed that chiral hinge modes are generic for a topological insulator in an external magnetic field.[28] Such hinge modes are not anomalous, however, because they can be removed by an appropriate surface decoration (see **Figure 5**b). For this reason, the hinge states of the $\mathcal{T}\mathcal{R}_4$-symmetric model of Equation (11) are *intrinsic*, whereas hinge states that appear in the absence of a crystalline symmetry are *extrinsic*.

Without the term proportional to Γ_4, the model (11) is not only invariant under time reversal and fourfold rotation, but it also satisfies three anticommuting mirror symmetries $\mathcal{M}_i : k_i \to -k_i$, with $U_{\mathcal{M}_i} = \Gamma_4\Gamma_i$, $i = 1, 2, 3$, and inversion symmetry $\mathcal{I} : \vec{k} \to -\vec{k}$, with $U_{\mathcal{I}} = \Gamma_0$. As the mass term Γ_4 is incompatible with each of these crystalline symmetries, imposing

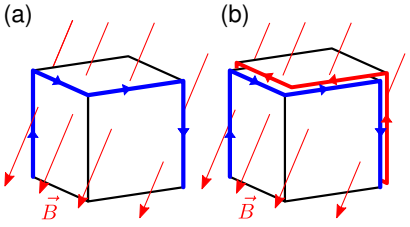

Figure 5. a) Schematic picture of an "extrinsic" second-order topological insulator consisting of a 3D topological insulator placed in a magnetic field in a generic direction, as proposed by Sitte et al.[28] Each surface has a finite flux and there are chiral modes along hinges that touch two faces with opposite sign of the magnetic flux. b) The gapless hinge modes may be removed by decorating some of the crystal faces with a two-dimensional anomalous quantized Hall insulator.

mirror or inversion symmetry while breaking $\mathcal{T}$ also results in a second-order topological phase for $-6t < m < 0$.[13,15,18–21]

3.4. Higher-Order Topological Phases

In general, a crystalline topological phase is called an nth-order topological phase if it has anomalous boundary signatures of codimension n if the boundary as a whole respects the crystalline symmetries. With this definition, a topological phase that does not rely on crystalline symmetries for its protection is a first-order topological phase. As topological phases without crystalline symmetries always have a first-order boundary signature, higher-order topological phases are necessarily crystalline topological phases. The aforementioned definition of the order of a topological crystalline phase assumes a crystal termination for which the codimension of the boundary states is maximal. For special choices of the termination, an nth order topological phase may have boundary signatures of codimension smaller than n. For example, a crystal with a face invariant under the point-group symmetry G hosts codimension-one boundary states if the bulk band structure has a nontrivial topology. For a higher-order topological phase, these codimension-one boundary states disappear for a generic orientation of the faces, leaving boundary states of a larger codimension behind (see **Figure 6**). In addition, as the example in **Figure 7**a,b shows, even with an identical orientation of the faces, a given crystal can exhibit boundary states of different codimensions depending on the details of the termination. Whereas for the former example, the convention of assigning the order of a phase according to the maximal codimension follows naturally from the observation that a termination without symmetry-invariant faces is more generic than the one with such faces, for the example in Figure 7a,b determining the order of the topological phase according to the maximal codimension of the anomalous boundary states is a matter of convention. Finally, we note that in the literature, topological phases with anomalous corner *charges* (as opposed to corner *states*) are sometimes also referred to as higher-order phases, although such obstructed atomic-limit phases fall outside the boundary-based classification scheme we will use in this review.

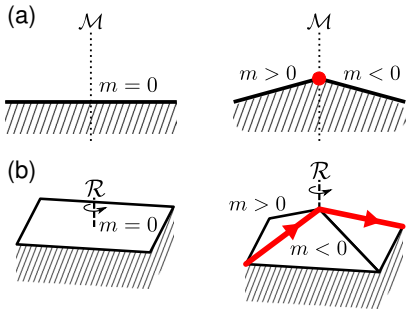

Figure 6. a) A 2D crystal with a mirror-symmetric edge, at which the mirror symmetry acts as a local symmetry (left) and a generic mirror-symmetric termination, at which the mirror symmetry acts as a "global" symmetry only (right). b) A 3D crystal with a rotation-invariant surface, at which the rotation symmetry acts as a local symmetry (left) and a generic fourfold rotation-symmetric termination, at which the rotation symmetry acts as a global symmetry (right). In both panels, a configuration of boundary mass terms is shown that corresponds to a second-order phase.

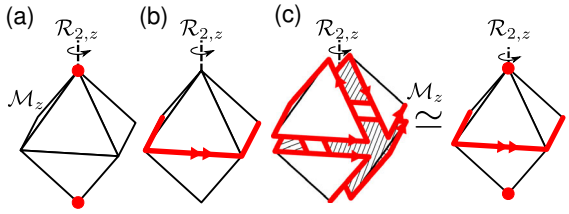

Figure 7. A topological 3D superconductor with mirror and twofold rotation symmetry admits a) Majorana corner modes at the rotation axis or b) a pair of copropagating Majorana hinge modes at the mirror plane. The difference between these two boundary signatures is a matter of crystal termination: c) The higher-order boundary modes in a crystal that has corner states as well as hinge modes are extrinsic.

(They are captured in the K-theory-based classification scheme of the bulk band structure.)

3.5. Experimental Realizations of Higher-Order Band Structures

The existence of corner modes in the BBH model was demonstrated experimentally in various classical systems. These include electrical[44,45] and microwave[46] circuits, as well as coupled mechanical oscillators.[47] Although the spatial symmetries and the chiral antisymmetry required to pin the frequency of the corner modes to the center of an excitation gap are not natural symmetries for these platforms, the near-complete control over device parameters ensures that these symmetries can be implemented experimentally to a sufficiently high degree. Corner modes of true quantum-mechanical origin were observed in an artificial electronic lattice obtained by placing CO molecules on a Cu(111) surface,[48] although the specific lattice model implemented in Kempkes et al.[48] has a topologically trivial band structure with accidental nonanomalous corner modes.

To date, experimental evidence of the higher-order topology of 3D band structures was reported for two materials only: elemental bismuth[49,50] and the Van der Waals material Bi_4Br_4.[51] In Bi_4Br_4, which is a 2D stacking of quasi-1D molecules, helical hinge states are protected by a twofold rotation symmetry along the molecular axis. Noguchi et al. demonstrate the existence of 1D hinge states in Bi_4Br_4 using angle-resolved photoemission spectroscopy,[51] a technical tour-de-force given the low dimensionality of the feature to be resolved spectroscopically. Hinge states in Bi are protected by inversion symmetry $\mathcal{I}$. Bismuth has an additional threefold rotation symmetry $\mathcal{R}_3$, leading to a characteristic hexagonal pattern of helical hinge states for a Bi flake cut perpendicular to the rotation axis (see **Figure 8**a). The experimental demonstration that Bi has a higher-order band structure is complicated by the fact that Bi is a semimetal with indirect band overlap. Evidence that Bi has a higher-order band structure is based on a measurement of the current-phase relationship for the Josephson current through Bi pillars,[49,52] which has a sawtooth-like contribution characteristic of ballistic 1D channels. The observation of 1D states at three out of six step edges of a hexogonal terrace on a Bi surface provides further evidence for the higher-order topology of the Bi band structure. This experimental signature is not unambiguous, however. Theoretically, for a terrace (as opposed to a free-standing flake)

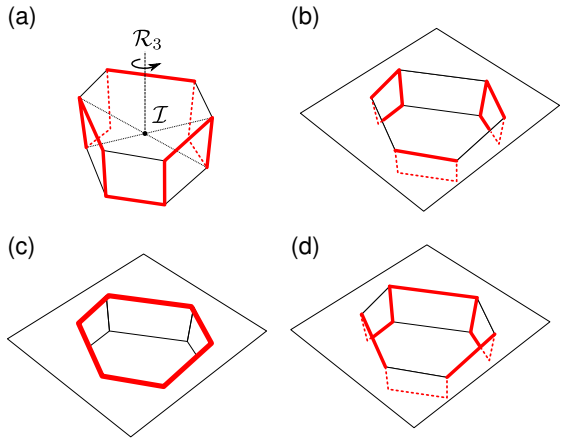

Figure 8. a) Hexagonal Bi pillar with threefold rotation axis, inversion center, and arrangement of anomalous hinge modes characteristic of a second-order band struture.[49] b) Hexagonal terrace with the edge states consistent with (a). c,d) Anomalous 1D modes at the edges of a one-atomic-layer high terrace on the surface of a weak topological insulator. Whether the 1D modes are centered at the upper or lower end of the terrace is not fixed by the weak topology alone and may depend on details of the termination or on the combined presence of weak and second-order topology.

one expects the pattern of edge modes shown in Figure 8b if the band structure has second-order topology. This is most easily seen in the domain-wall picture (see Section 3.6) by observing that each crystal face has a well-defined sign of its unique surface mass term that depends on the orientation of that surface only. Note that upon placing the flake of Figure 8a into the terrace of Figure 8b it appears as if an odd number of hinge modes are left behind, as in Figure 8c. This is not the case. Inclusion of the hopping between the flake and the terrace closes and reopens the surface gaps at the boundary between the flake and the terrace, which removes these hinge states. This is analogous to the situation that occurs when placing the two copies of the flake from Figure 8a on top of each other. The presence of an even number of modes at each edge of the terrace means that the edge modes no longer have topological protection if the terrace is only one or a few atomic layers thick. Based on scanning tunneling spectroscopy experiments close to a screw dislocation, Nayak et al.[50] find that Bi has a nontrivial weak topology. With weak topology, which may or may not occur in combination with second-order topology of the bulk band structure, a one-atomic-layer high step edge hosts an odd number of helical modes. The mode patterns corresponding to weak topology, such as those of Figure 8c,d, may be difficult to distinguish experimentally from the mode pattern of Figure 8b.

3.6. Domain-Wall Picture

To understand why a topological band structure with crystalline symmetries can give rise to higher-order boundary states, previous studies[15,18–21] propose a "domain-wall picture." In its original form, the domain-wall picture applies if the crystalline symmetry group G admits a boundary orientation that is invariant under G. This is the case, for example, for a mirror symmetry in 2D or for a rotation symmetry in 3D (see Figure 6). For such an invariant boundary, the crystalline symmetry continues to act as a *local* symmetry at the boundary. Therefore, the bulk–boundary correspondence for nonspatial symmetries is applicable and guarantees the existence of an anomalous boundary state on that crystal face. The low-energy theory of that anomalous $(d-1)$-dimensional boundary state has the form of a Dirac Hamiltonian

$$H_\partial(k_1, \ldots, k_{d-1}) = \sum_{i=1}^{d-1} \gamma_i k_i \tag{14}$$

with anticommuting gamma matrices $\gamma_i^2 = 1$, $i = 1, \ldots, d-1$. Again, we search for anticommuting mass terms $\mu_j^2 = 1$ with $\{\mu_j, \gamma_i\} = 0, i = 1, \ldots, d-1, j = 1, \ldots, n$. If the bulk topological phase is not a first-order phase, there must be at least one such mass term. The mass terms transform under a real representation O_n of the crystalline symmetry group G, which cannot be the trivial representation, because otherwise H_∂ can be gapped out by a symmetry-preserving perturbation.

Higher-order boundary states appear when we consider deformations of the invariant boundary, so G no longer acts locally but continues to act on the crystal boundary as a whole. Examples of such deformations are shown in Figure 6. Given the number n of mass terms and the representation O_n of G, one can derive the pattern of anomalous higher-order boundary states. Such boundary states are of second order if $d = 2$. They are also of second order if $d = 3$ and $n = 1$ or if G leaves a 1D subset of the deformed crystal face invariant (as is the case of, e.g., a mirror symmetry). Otherwise the boundary states are of third order in 3D.

A "trick" to extend this argument to symmetry groups G without invariant boundary orientation, such as inversion symmetry, was proposed in Geier et al.[18] The trick involves considering a $(d+1)$-dimensional topological crystalline band structure with a symmetry group G' obtained by acting with G on the first d coordinates, while leaving the $(d+1)$th coordinate unchanged. For the $(d+1)$-dimensional crystal, the conditions of the domain-wall argument are obviously fulfilled, so one can establish the existence of higher-order boundary states using the domain-wall picture outlined previously. Geier et al. [18] then make use of an isomorphism between $(d+1)$-dimensional topological band structures with symmetry group G' and d-dimensional topological band structures with symmetry group G that was originally derived for noncrystalline topological phases by Fulga et al.[53] As this isomorphism preserves the order of the anomalous boundary states,[12,18] one can directly infer the existence of higher-order boundary states for the d-dimensional crystal with symmetry group G.

As an example, we consider the crystal described by Equation (11). The $\mathcal{T}\mathcal{R}_4$ symmetry leaves surfaces at constant z invariant. The low-energy surface Hamiltonian has the form

$$H_\partial(k_1, k_2) = k_1\gamma_1 + k_2\gamma_2 \tag{15}$$

with $\gamma_1 = \sigma_1$ and $\gamma_2 = \sigma_3$. The surface Hamiltonian H_∂ satisfies the product $\mathcal{T}\mathcal{R}_4$ of time-reversal and fourfold rotation symmetry

$$H_\partial(k_1, k_2) = U_{\mathcal{T}\mathcal{R}} H_\partial(-k_2, k_1)^* U_{\mathcal{T}\mathcal{R}}^\dagger \tag{16}$$

with $U_{\mathcal{TR}} = e^{-i\pi\sigma_2/4}$. There is a single mass term $\mu = \sigma_2$, which changes sign under $\mathcal{TR}_4$. If one then deforms the invariant surface as in Figure 6b, the faces related by fourfold rotation have opposite masses, so there are domain walls with a sign change of the mass term at "hinges" between these faces.[13] The gapless chiral modes run along the domain walls. The same argument can be used if the model (11) is considered with a mirror symmetry $\mathcal{M}_x$ or $\mathcal{M}_y$ instead of with $\mathcal{TR}_4$ symmetry.[13,15]

3.7. Boundary States from Dirac-Like Bulk Hamiltonian

The low-energy Dirac theory of the boundary and the transformation behavior of the boundary mass terms under the crystalline symmetry group can be obtained by direct calculation from the Dirac-like form of the bulk band structure. The starting point is the $2b$-band Dirac Hamiltonian

$$H(\vec{k}) = m\Gamma_0 + \sum_{j=1}^{d} k_j \Gamma_j \tag{17}$$

which is, for example, the low-energy limit of the models (1), (10), or (11). Here the matrices Γ_j are mutually anticommuting $2b \times 2b$ matrices that satisfy $\Gamma_j^2 = 1$, $j = 0, 1, \ldots, d$.

The crystal boundary is modeled as the interface between regions with negative and positive m, with m negative in the interior of the crystal. Near the sample boundary, the Hamiltonian (Equation (17)) has the form

$$H = m(x_\perp)\Gamma_0 - i\hbar\vec{\Gamma}\cdot\partial_{\vec{r}} \tag{18}$$

where $x_\perp = \vec{n}\cdot\vec{r}$ is the coordinate transverse to the boundary, $\vec{n}$ is the outward-pointing normal, and $\vec{\Gamma}$ is a d-component vector containing the matrices Γ_j, $j = 1, \ldots, d$. We choose $m(x_\perp) > 0$ for $x_\perp > 0$ and $m(x_\perp) < 0$ for $x_\perp < 0$, so that the sample interior corresponds to negative $x_\perp$. The Hamiltonian (Equation (18)) admits b gapless boundary modes, the projection operator to the space of allowed $2b$-component spinors being

$$P(\vec{n}) = \frac{1}{2}[i(\vec{n}\cdot\vec{\Gamma})\Gamma_0 + 1] \tag{19}$$

The effective b-band low-energy surface Hamiltonian is obtained using the projection operator $P(\vec{n})$. To illustrate this procedure, we consider a hypothetical circular or spherical "crystal" of radius R and use the polar coordinate ϕ or spherical coordinates (θ, φ) to parameterize $\vec{n}$ and the crystal boundary for $d = 2$ or $d = 3$, respectively.[19] We write the projection operator (Equation (19)) as

$$P(\vec{n}) = V_d(\vec{n})P_d V_d(\vec{n})^{-1}, \quad d = 2, 3 \tag{20}$$

with $P_2 = P(\vec{e}_x)$, $P_3 = P(\vec{e}_z)$, $V_2(\vec{n}) = e^{\phi\Gamma_2\Gamma_1/2}$, and $V_3(\vec{n}) = e^{(\pi-\theta)\Gamma_1\Gamma_3/2}e^{\varphi\Gamma_2\Gamma_1/2}$. The projected Hamiltonian H at the boundary then reads

$$P(\vec{n})HP(\vec{n}) = V_2(\vec{n})P_2\left(-i\Gamma_2\frac{1}{R}\frac{\partial}{\partial\phi}\right)P_2 V_2(\vec{n})^{-1} \tag{21}$$

if $d = 2$ and

$$P(\vec{n})HP(\vec{n}) = V_3(\vec{n})P_3 \times \left(-i\Gamma_1\frac{1}{R}\frac{\partial}{\partial\theta} - i\Gamma_2\frac{1}{R\sin\theta}\frac{\partial}{\partial\varphi}\right) \times P_3 V_3(\vec{n})^{-1} \tag{22}$$

if $d = 3$. Mass terms M_i, $i = 1, \ldots, n$, of the bulk band structure (Equation (17)) may be added as a position-dependent perturbation to the surface. Although such mass terms locally violate the crystalline symmetry group G, the position dependence of the surface perturbation ensures compatibility with G for the crystal as a whole. The matrices $\gamma_2 = P_2\Gamma_2 P_2$ (for $d = 2$) or $\gamma_{1,2} = P_3\Gamma_{1,2}P_3$ (for $d = 3$), combined with $\mu_j = P_d M_j P_d$, $j = 1, \ldots, n$, form a set of anticommuting gamma matrices and mass terms of effective dimension b. This gives the effective boundary Hamiltonian

$$\begin{aligned} H_\partial &= \gamma_2\left(-i\frac{1}{R}\frac{\partial}{\partial\phi}\right) + \sum_{j=1}^{n} m_j(\phi)\mu_j, \quad d = 2 \\ H_\partial &= \gamma_1\left(-i\frac{1}{R}\frac{\partial}{\partial\theta}\right) + \gamma_2\left(-i\frac{1}{R\sin\theta}\frac{\partial}{\partial\varphi}\right) \\ &\quad + \sum_{j=1}^{n} m_j(\theta,\varphi)\mu_j, \quad d = 3 \end{aligned} \tag{23}$$

The position dependence of the prefactors m_j must be chosen such that the boundary Hamiltonian H_∂ as a whole is compatible with the crystalline symmetry group G. Hereto, we note that the induced representation u_g of the crystalline symmetry operation g on the boundary Hamiltonian gives an n-dimensional real representation O_n of G

$$u_g\mu_j u_g^{-1} = \sum_{j'=1}^{n} (O_n(g))_{jj'}\mu_{j'} \tag{24}$$

so compatibility with the crystalline symmetry group is ensured if the functions m_j satisfy the requirements

$$m_j(\vec{n}) = \sum_{j'=1}^{n} m_{j'}(g\vec{n})O_n(g)_{j'j}. \tag{25}$$

As a first example, we illustrate this procedure for the BBH model (4). If the BBH model is written in the form of Equation (10), a low-energy Dirac Hamiltonian of the form of Equation (17) is immediately obtained. There is only one mass term $M = \Gamma_4$ that is invariant under particle–hole conjugation $\mathcal{P}$ or the chiral antisymmetry $\mathcal{C}$. This mass term changes sign under the fourfold rotation operation $\mathcal{R}_4$. It follows that the boundary Hamiltonian H_∂ is of the form of Equation (23) with the condition

$$m(\phi + \pi/2) = -m(\phi) \tag{26}$$

to ensure compatibility with respect to $\mathcal{R}_4$. The condition (26) implies the existence of four "domain walls" at which $m(\phi)$ changes sign. These domain walls each host an anomalous zero-energy state.

The second example (which will be considered again in Section 5) is a 3D odd-parity superconductor with point group C_{2h},

which is generated by commuting twofold rotation and mirror symmetries $\mathcal{R}_{2,z}$ and $\mathcal{M}_z$. The rotation symmetry is around the z axis; the mirror reflection is in the xy plane (see Figure 7). Using the convention that both crystalline symmetries square to one, $\mathcal{R}_{2,z}/\mathcal{M}_z$ commute/anticommute with particle–hole conjugation $\mathcal{P}$, respectively. This model is described by an eight-band Dirac Hamiltonian of the form of Equation (17) with $\Gamma_0 = \tau_2\sigma_0\rho_0$, $\Gamma_1 = \tau_1\sigma_3\rho_0$, $\Gamma_2 = \tau_1\sigma_1\rho_0$, and $\Gamma_3 = \tau_3\sigma_0\rho_0$. The relevant symmetries are represented by , $U_{\mathcal{P}} = 1$, $U_{\mathcal{M}} = \tau_2\sigma_2\rho_2$, and $U_{\mathcal{R}} = \tau_0\sigma_2\rho_2$. There are two $\mathcal{P}$-symmetric mass terms that break the crystalline symmetry: $M_1 = \tau_1\sigma_2\rho_1$ and $M_2 = \tau_1\sigma_2\rho_3$. Both mass terms are symmetric under $\mathcal{M}_z$ but antisymmetric under $\mathcal{R}_{2,z}$. Therefore, the effective surface theory is of the form of Equation (23) with the condition

$$m_j(\theta, \varphi) = -m_j(\theta, \varphi + \pi), \quad j = 1, 2 \tag{27}$$

Such a mass term has a singular "vortex"-like structure at the poles at $\theta = 0$, π, resulting in the presence of protected zero modes there (see Figure 7a). There are no protected second-order boundary states, as generically at least one of the two mass terms is nonzero away from the poles.

It is interesting to point out that in this example one could also have chosen the single mass term $M = \tau_1\sigma_2\rho_0$. This mass term does not admit any further anticommuting mass terms. As M is odd under $\mathcal{M}_z$ but even under $\mathcal{R}_{2,z}$, one would then have concluded that this model has a pair of copropagating chiral Majorana modes at the mirror plane (see Figure 7b). The difference between this boundary signature and the third-order boundary signature with Majorana zero modes at the twofold rotation axis is extrinsic, because it corresponds to a trivial bulk band structure. Indeed, by explicit construction, one verifies that it is possible to construct a boundary decoration that has Majorana corner modes at the rotation axis and two copropagating chiral modes at the mirror plane (see Figure 7c). Addition o f this boundary decoration switches between the boundary signatures of Figure 7a,b. As the codimension-2 boundary signature of Figure 7b can be eliminated in favor of the codimension-3 boundary of Figure 7a by a suitable choice of termination, this model must be considered a *third-order* topological band structure.

3.8. Boundary-Resolved Classification

The K-theory classification classifies topological band structures without considering boundary signatures. In general, the classifying group K for a given combination of nonspatial and crystalline symmetries contains first-order topological phases, which do not rely on the presence of the crystalline symmetries for their protection, higher-order topological phases, as well as atomic-limit phases that do not have protected boundary states, but may or may not have boundary charges. To obtain a boundary-resolved classification, Trifunovic and Brouwer[21] propose to consider a subgroup sequence

$$K^{(d)} \subset K^{(d-1)} \subset \ldots \subset K^{(1)} \subset K \tag{28}$$

where $K^{(n)}$ contains those elements of K that do not have intrinsic boundary signatures of order n or lower (see **Figure 9** for a schematic illustration). One verifies that $K^{(n)}$ is indeed a subgroup of K, because the "addition" of band structures (i.e., taking the direct sum) cannot lower the order of the boundary signatures. In the language used earlier, this conclusion follows from the observation that under taking direct sums the number of boundary mass terms does not decrease. The quotient $K^{(n+1)}/K^{(n)}$ classifies topological crystalline band structures with exactly n boundary mass terms on. Many of the examples discussed previously are generators of the topological classes in these quotient groups.

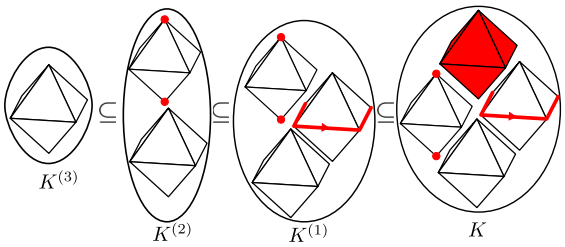

Figure 9. The K-theory classifying group K classifies all bulk band structures, regardless of their boundary signature. Refined classification groups $K^{(n)}$ are defined by excluding topological phases with anomalous boundary states of order $\leq n$. The figure illustrates this procedure for a crystal with inversion symmetry $\mathcal{I}$, showing generators only. Anomalous boundary states are indicated in red.

To illustrate the use of the boundary-resolved classification (Equation (28)), we give the subgroup sequences for 1D inversion-symmetric odd-parity superconductors, of which the "Kitaev chain" (Equation (1)) is an example

$$2\mathbb{Z} \subset \mathbb{Z} \tag{29}$$

and for 2D superconductors with fourfold rotation symmetry $\mathcal{R}_4$

$$\mathbb{Z} \times 2\mathbb{Z} \subset \mathbb{Z}^2 \subset \mathbb{Z}^3 \tag{30}$$

of which the BBH model (4) is an example. These equations summarize the discussions of the boundary-resolved classifications of the last paragraphs of Sections 3.1 and 3.2, respectively.

4. Bulk–Boundary Correspondence for Topological Crystalline Phases

The bulk–boundary correspondence relates the topological classification of anomalous boundary states to the boundary-resolved classification (Equation (28)) of the bulk band structure. It states i) that

$$\mathcal{K}_{\mathrm{a}}^{(n)} = K^{(n-1)}/K^{(n)} \tag{31}$$

where $\mathcal{K}_{\mathrm{a}}^{(n)}$ is the classification group of anomalous nth-order boundary states and $K^{(n)}$ is the K-theory classification group of topological band structures without an intrinsic boundary signature of order $\leq n$ and ii) that the topological crystalline band structures without an anomalous boundary signature, which are classified by $K^{(d)}$, can be continuously deformed to atomic-limit phases. Trifunovic and Brouwer[21] derive these relations using

algebraic methods for order-two crystalline symmetries, crystalline symmetries that square to one. Such a general derivation is possible because of the existence of a complete K-theory classification in this case.[11] We will discuss a heuristic derivation of the bulk–boundary correspondence for a general point group G at the end of this section.

The formal definition of the classifying group $\mathcal{K}_a$ of anomalous higher-order boundary states and a method to compute it are shown in Section 4.1. The right-hand side of the bulk–boundary correspondence (Equation (31)) contains the subgroups $K^{(n)}$ of the classifying group of topological crystalline band structures K that classify the higher-order band structures. Such a refined bulk classification is obtained by an extension of the method introduced by Cornfeld and Chapman,[43] as explained in Section 4.2. A constructive proof of the bulk–boundary correspondence (Equation (31)) consists of independent calculations of the left- and right-hand side of Equation (31) for a given symmetry group. Here, one needs to not only demonstrate a one-to-one correspondence between the two groups in Equation (31), but also that the generators of the groups $K^{(n-1)}/K^{(n)}$ have the corresponding anomalous boundary states once terminated. As the presence or absence of anomalous boundary states is a topological property, this verification can be performed for a convenient choice of the bulk band structure and the termination, such as the low-energy Dirac-like Hamiltonians with smooth terminations, for which we can use the domain-wall picture of Section 3.6.

4.1. Anomalous Boundary States

The classification group $\mathcal{K}_a^{(n)}$ classifies anomalous nth-order boundary states for a crystal shape that is compatible with the crystalline symmetry group G. We use the convention that the sum of an nth-order boundary state and boundary state of order larger than n is considered a boundary state of order n. The precise definition of the group $\mathcal{K}_a^{(n)}$ requires the notion of the G-symmetric cellular decomposition of a crystal:[54] Denoting the interior of the crystal by X, one writes

$$X = \mathbf{\Omega}_0 \cup \mathbf{\Omega}_1 \cup \ldots \cup \mathbf{\Omega}_d \tag{32}$$

where d is the spatial dimension and $\mathbf{\Omega}_k$ is a set of disjoint "k-cells" c_k—a k-cell is a k-dimensional subset of X that is homotopic to the interior or a k-dimensional sphere—which have the property that each element $g \in G$ either leaves each point in c_k invariant or bijectively maps the k-cell c_k to a different k-dell $c_{k'}$. Further, for a pair of k-cells c_k and $c_{k'}$ in $\mathbf{\Omega}_d$ there is one and precisely one $g \in G$ that maps these cells onto each other. Examples of G-symmetric cellular decompositions are shown in **Figure 10** for a crystal with inversion symmetry and for a crystal with mirror and twofold rotation symmetries.

To construct topological boundary states of dimension $k-1$, we first consider the allowed k-dimensional topological phases with support on the k-cell c_k. As the only relevant symmetries acting within c_k are local—recall that each element $g \in G$ either leaves each point in c_k invariant or it does not act inside c_k—any topological phase placed on c_k satisfies the standard bulk–boundary correspondence. This establishes a one-to-one correspondence between topological phases with support on c_k and

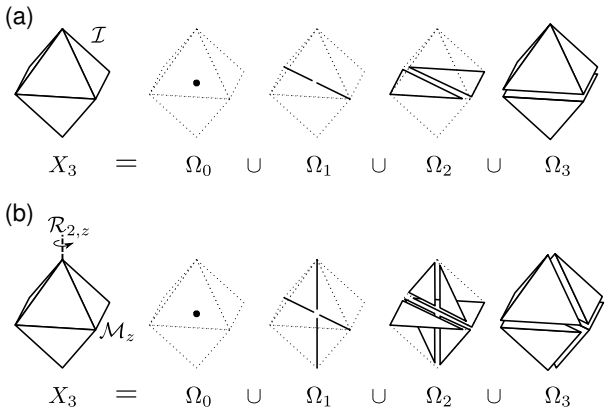

Figure 10. G-symmetric cellular decompositions of the octahedron for the crystalline symmetry group a) G generated by inversion $\mathcal{I}$ and for b) $G = C_{2h}$, generated by mirror $\mathcal{M}_z$ and twofold rotation symmetry $\mathcal{R}_{2,z}$.

boundary states at its boundary ∂c_k. By placing k-dimensional topological phases on $\mathbf{\Omega}_k$ in a G-compatible manner, we can generate protected $(k-1)$-dimensional states on the crystal boundary ∂X, provided any topological boundary states that arise in the interior of the crystal mutually gap out. This procedure gives a construction of all topological boundary states on $\partial\mathbf{\Omega}_k \cap \partial X$, both extrinsic and intrinsic. As its "building blocks," topological phases defined on the k-cells, have a classification with a well-defined group structure, the result of this procedure has a group structure, too. Setting $k = d+1-n$, we refer to it as $\mathcal{K}^{(n)}$, the classifying group of all n-th order topological boundary states on $\partial\mathbf{\Omega}_{d+1-n} \cap \partial X$. Note that, in principle, codimension-n boundary states may also appear outside $\partial\mathbf{\Omega}_{d+1-n}$, but such states can be moved to $\partial\mathbf{\Omega}_{d+1-n}$ by a suitable change of crystal termination along $d+1-n$-dimensional crystal faces (see **Figure 11**).

Let us now apply the above general considerations for the example of the point groups $G = C_i$ (inversion), for which the

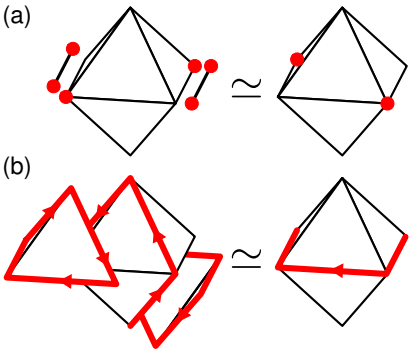

Figure 11. By attaching a "decoration" consisting of a first-order topological phase on a boundary of codimension $n-1$, an arbitrary configuration of boundary state of codimension n can be moved to the subset $\partial\mathbf{\Omega}_{d+1-n} \cap \partial X$. The figure shows two examples for a 3D crystal with inversion symmetry: a) Corner states at generic corners can be moved to $\partial\mathbf{\Omega}_1$ by changing the crystal termination along two crystal hinges and b) hinge states at a generic hinge can be moved to $\partial\mathbf{\Omega}_2$ by changing the crystal termination at two crystal faces. In both cases, the hinges or faces at which the termination is changed are related by inversion.

cellular decomposition is shown in Figure 10a. (A second example, corresponding to $G = C_{2h}$—see Figure 10b—will be discussed in Section 5.1.) The first-order boundary states are generated and classified by placing a 3D tenfold-way phase onto one of the two 3-cells in $\mathbf{\Omega}_3$ (provided nontrivial phases for the tenfold-way class of interest). An inverted copy of this phase on the other 3-cell ensures that the crystal as a whole is inversion-symmetric. The resulting phase has inversion-symmetric first-order boundary states if the pair of surface states in the interior of the crystal can be mutually gapped out. Similarly, to generate all second-order boundary states, we place a 2D tenfold-way phase and an inverted copy on the two 2-cells in $\mathbf{\Omega}_2$. This way an order-two boundary state is obtained, provided the two 1D states along the interior boundary between the two 2-cells gap out. Third-order boundary states are constructed analogously by placing tenfold-way phases onto the two 1-cells in $\mathbf{\Omega}_1$.

This construction gives the classifying group $\mathcal{K}^{(n)}$ of *all* nth order topological boundary states, both intrinsic and extrinsic. To find the classifying group $\mathcal{K}_{\mathrm{a}}^{(n)}$ of anomalous (i.e., intrinsic) nth order boundary states, one has to divide out the subgroup $D^{(n)} \subset \mathcal{K}^{(n)}$ of extrinsic boundary states, i.e., of topological states on $\partial\mathbf{\Omega}_{d+1-n} \cap \partial X$ that appear as the boundary states of topological phases with support entirely within the crystal boundary ∂X. To classify such states that can be obtained by "decoration" of the crystal boundary ∂X, we make use of the induced G-symmetric cellular decomposition of the boundary ∂X

$$\partial X = \mathbf{\Omega}_0^{\partial} \cup \mathbf{\Omega}_1^{\partial} \cup \ldots \cup \mathbf{\Omega}_{d-1}^{\partial} \tag{33}$$

where $\mathbf{\Omega}_k^{\partial} = \mathbf{\Omega}_{k+1} \cap \partial X$. **Figure 12** shows the induced G-symmetric cellular decomposition of the crystal boundaries for the examples discussed earlier. Proceeding as before, all boundary states classified by $D^{(n)}$ can be obtained by "pasting" nontrivial topological phases (with the appropriate local symmetries, if applicable) onto k-cells $\mathbf{\Omega}_k^{\partial}$ with $k \geq d+1-n$, with the requirement that all the states of dimension $> d-n$ can be gapped out. The classifying group $\mathcal{K}_{\mathrm{a}}^{(n)}$ of anomalous nth-order boundary states is then

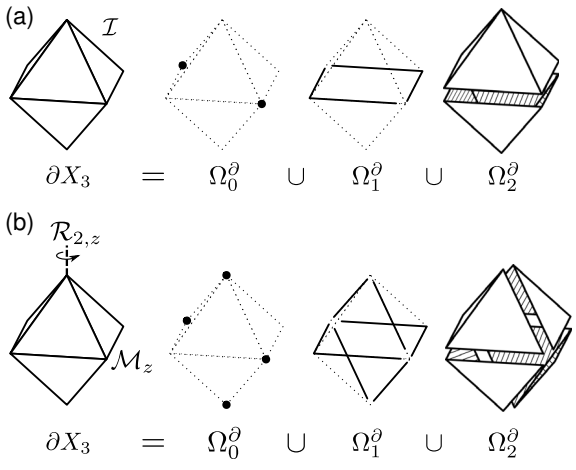

Figure 12. G-symmetric cellular decompositions of the boundary of an octahedron for a) G generated by inversion $\mathcal{I}$ and b) for $G = C_{2h}$ generated by mirror- and twofold rotation symmetry.

$$\mathcal{K}_{\mathrm{a}}^{(n)} = \mathcal{K}^{(n)}/\mathcal{D}^{(n)} \tag{34}$$

The importance of considering decorations by phases of dimension larger than $d+1-n$ is that one should also consider decorations with higher-order topological phases with support on the crystal boundary. Trifunovic and Brouwer[21] discuss an example for which this is relevant: a 3D inversion-symmetric time-reversal invariant superconductor. For this example, the classifying group $\mathcal{K}^{(3)} = \mathbb{Z}_2$ is generated by a boundary state consisting of two Majorana–Kramers pairs positioned on the boundary 0-cell $\mathbf{\Omega}_0^{\partial}$ (see Figure 12a). Such a configuration of Majorana–Kramers pairs can also be obtained from a standalone 2D $\mathcal{T}$-symmetric superconductor with support on the crystal surface: In the G-symmetric cellular decomposition of the boundary, the two 2-cells in $\mathbf{\Omega}_2^{\partial}$ host a 2D $\mathcal{T}$-symmetric superconductor with helical Majorana modes. The two helical Majorana modes gap out at the interface between the two 2-cells, leaving behind Kramers–Majorana zero modes at two inversion-related corners.

To make this construction more specific, we will apply it to the example of an odd-parity topological superconductor with crystalline symmetry group C_{2h} in Section 5.

4.2. Refined Bulk Classification

Close to a phase transition between two different topological phases, the low-energy description of the band structure can be chosen to take the Dirac form (Equation (17)). As we are interested in classifying strong phases that are protected by the point-group symmetry G, we may assume that the gap closing appears in the center of the Brillouin zone. For this reason, the (strong) topological classification of band structures is the same as the classification of Dirac Hamiltonians.

The key simplifying observation is that close to the phase transition, the low-wavelength description of the band structure is very "symmetric" and allows the classification problem with point-group symmetries to be mapped to a classification problem with local (i.e., onsite) symmetries or antisymmetries only.[11,43,55] With an onsite symmetry group G, the Dirac Hamiltonian can be block-diagonalized, where each "block" is labeled by an irreducible representation of G. The individual blocks are no longer constrained by point-group symmetries but only by nonspatial symmetries that have same mathematical form as the fundamental symmetries $\mathcal{P}$, $\mathcal{T}$, and/or $\mathcal{C}$. Therefore, each block corresponds to one of the tenfold-way classes, the classification of which is well known.[5,6] The realization of a mapping between point-group symmetries and onsite symmetries was first provided by Shiozaki and Sato for order-two symmetries,[11] and later extended by Cornfeld and Chapman to all point-group symmetries.[43] Subsequently we refer to this mapping as the "Cornfeld–Chapman isomorphism."

Once the topological classification K of gapped Dirac Hamiltonians is known, the next task is to refine this classification according to the boundary signatures of the different phases (Equation (28)). This requires finding mass terms that are incompatible with the crystalline symmetry group G and evaluating the order of the boundary state associated with their transformation behavior under G. A complication is that there

may be multiple choices for the mass terms with different numbers of mass terms and/or different order of the associated boundary signatures. If this complication occurs, the difference of boundary signatures that correspond to different choices of the mass terms is *extrinsic*; that is, it is associated with a topological trivial bulk.

To find a proper correspondence between a Dirac Hamiltonian and its boundary signature, the configuration of mass terms with the maximal order of the boundary states has to be found. For simple examples, this is most easily accomplished by inspection of the Dirac Hamiltonians corresponding to the generators of K, as was done in the examples discussed in Section 3. We now discuss a systematic procedure that gives the same result.

The calculation of the subgroup $K^{(n)}$ of topological phases with a boundary signature of order not lower than n proceeds in two steps. First one selects all n-dimensional real (but not necessarily irreducible) representations O_n of the point group G that correspond to $(n+1)$th-order boundary signatures if n mass terms M_1, ..., M_n were to transform under G with the representation O_n. Second, the classification group K_{O_n} for Dirac Hamiltonians with mass terms that transform under G in this manner is obtained. As Dirac Hamiltonians in K_{O_n} satisfy the full crystalline symmetry group G if the mass terms M_1, ..., M_n are omitted, there is a natural inclusion $K_{O_n} \rightarrowtail K$. The subgroup $K^{(n)} \subset K$ is generated by the group $K^{(n+1)}$ and by the images $K_{O_n} \rightarrowtail K$, from all the representations selected in the first step.

The aforementioned procedure is simplified by the following two observations: First, the calculation of $K^{(d)}$, which is needed as a starting point, is achieved using the observation made by Shiozaki[56] that it is sufficient to consider only a single representation of the point group, the "vector representation" O_d^{vec}, in which the mass terms M_1, ..., M_d transform in the same way as the position vector. Shiozaki proved this statement by showing that $K_{O_d^{\mathrm{vec}}}$ is isomorphic to the classification of 0D phases placed onto $\mathbf{\Omega}_0$, taking into account the symmetry restrictions imposed by the full crystalline symmetry group, which acts onsite on $\mathbf{\Omega}_0$. As all atomic-limit phases, in presence of wallpaper or space group constraints, are obtained by placing 0D phases on different Wyckoff positions,[21,34,57] which for the case of point-group symmetries reduce to a single position $c_0 \in \mathbf{\Omega}_0$, one concludes that the image of $K_{O_d^{\mathrm{vec}}} \rightarrowtail K$ is precisely $K^{(d)}$. For example, a 2D system with mirror symmetry does not have topologically nontrivial atomic limits as $\mathbf{\Omega}_0$ is empty, while for a 3D system with inversion symmetry the nontrivial atomic limits are obtained by placing a 0D inversion-symmetric Hamiltonian on the inversion-symmetric point in $\mathbf{\Omega}_0$ (see Figure 10a). The second observation concerns the calculation of $K^{(1)}$, which classifies Dirac Hamiltonians that are trivialized once the constraints posed by the point-group symmetries are lifted. This group is most easily computed as the kernel of the inclusion $K \rightarrowtail K_{\mathrm{TF}}$, where K_{TF} is the tenfold-way classifying group without point-group constraints. This way, the bulk subgroup sequence (Equation (28)) is readily obtained for $d = 1, 2$. In three spatial dimensions, the only additional task that needs to be accomplished is the computation of the subgroup $K^{(2)}$, which requires considering all 2D real representations O_2 corresponding to third-order boundary signatures.

4.3. Heuristic Proof of Bulk–Boundary Correspondence

The statement that the bulk classifying group $K^{(d)}$ of topological crystalline band structures without anomalous boundary signatures precisely describes the atomic-limit phases follows from the observation that the absence of anomalous boundary signatures implies that a crystal can be smoothly "cut" into smaller subunits without generating gapless modes at interfaces. Performing this cutting procedure in a periodic manner gives the desired connection to an atomic-limit phase.

For the proof of the relation (31) the only nontrivial part is the surjectivity of the map $K^{(n-1)}/K^{(n)} \to \mathcal{K}_{\mathrm{a}}^{(n)}$. In this regard, we note that the construction of the classifying group $\mathcal{K}^{(n)}$ in Section 4.1 entails that all (anomalous) states on the boundary of a G-symmetric crystal X can be obtained by "embedding"[58] $(d+1-n)$-dimensional topological phases onto $(d+1-n)$-cells from the element $\mathbf{\Omega}_{d+1-n}$ of its G-symmetric cellular decomposition. It remains to be demonstrated that such "embedded" phases can be made translationally invariant. For order-two symmetries, this was proven with an algebraic method that constructs topological crystalline band structures with a Dirac low-energy description for a given element from $\mathcal{K}_{\mathrm{a}}^{(n)}$.[21] Alternatively, for order-two symmetries one can invoke a layer-stacking construction.[59,60] For an arbitrary symmetry group G, Huang et al. and Song et al.[61,62] propose the "topological crystal construction,"[61] in which X is viewed as a G-symmetric unit cell of a periodic lattice, which is repeated periodically in space. In comparison to the construction of Section 4.2 this construction imposes one additional condition: Boundary states at the "seam" between neighboring unit cells have to be gapped out. To the best of our knowledge, there is no proof that this condition is always met for an arbitrary symmetry group G, although we do not know of any counterexamples.

Alternatively, the bulk–boundary correspondence (Equation (31)) can be proven by independently calculating the bulk subgroup sequence and boundary classification using the methods reviewed in Sections 4.1 and 4.2. In the following section, we illustrate this procedure on one example.

5. Example: Odd-Parity Superconductor

To make the construction of Sections 4.1 and 4.2 more explicit, we apply it to the example of an odd-parity topological superconductor with a crystalline symmetry group C_{2h} (the point group generated by mutually commuting twofold rotation symmetry $R_{2,z}$ and mirror symmetry $\mathcal{M}_z$). Using the convention $\mathcal{R}_{2,z}^2 = \mathcal{M}_z^2 = 1$, $\mathcal{M}_z$ anticommutes with particle–hole conjugation $\mathcal{P}$, and $\mathcal{R}_{2,z}$ commutes with $\mathcal{P}$. An eight-band Dirac Hamiltonian for this symmetry class was discussed and analyzed in Section 3.7.

We conduct the constructive proof of the bulk–boundary correspondence (Equation (31)). In Section 5.1 we first obtain the left-hand side of Equation (31), the classification of anomalous higher-order boundary states. In Section 5.2 we subsequently compute the classification group K of topological crystalline bulk band structures and its subgroups $K^{(n)}$, which classify higher-order band structures. The bulk classification

provides generators of Dirac-like form, for which we find the anomalous boundary signatures using domain-wall picture. Together, these three steps give a constructive proof of the bulk–boundary correspondence (Equation (29)) for this symmetry class.

5.1. Boundary Classification

We first show that the boundary classification for this example is

$$\mathcal{K}_a^{(1)} = 0, \quad \mathcal{K}_a^{(2)} = 0, \quad \mathcal{K}_a^{(3)} = \mathbb{Z}_2 \tag{35}$$

Calculation of the boundary classification groups requires the G-symmetric cellular decompositions of the crystal and the crystal boundary, which are shown in Figure 10b and 12b, respectively. The result for $\mathcal{K}^{(1)}$ follows immediately, as there are no first-order boundary states—there are no nontrivial 3D superconductors that can be placed onto 3-cells in $\mathbf{\Omega}_3$.

Second-order boundary states may be obtained by placing 2D topological superconductors with chiral Majorana edge modes on the two 2-cells in the mirror plane or on the four 2-cells perpendicular to the mirror plane (see **Figure 13**a,b). In the former case, the local $\mathcal{M}_z$ symmetry imposes that the number of chiral Majorana modes of each of the two topological phases is even, because $\mathcal{M}_z$ anticommutes with $\mathcal{P}$. At the interior "seam" between the two 2-cells in the mirror plane, the Majorana modes are counterpropagating and can be gapped out. Therefore, placing topological phases at the 2-cells in the mirror plane results in a topological boundary state consisting of two copropagating chiral Majorana modes in the mirror plane. The classifying group of such boundary states is $2\mathbb{Z}$, the same as the classification group of 2D topological superconductors with an onsite symmetry anticommuting with $\mathcal{P}$.[21] Placing 2D topological superconductors with chiral Majorana edge modes on the four 2-cells perpendicular to the mirror plane does not result in a valid topological boundary state, as the chiral Majorana modes are copropagating at the rotation axis and cannot be gapped out there (see Figure 13b). We thus conclude that for this example $\mathcal{K}^{(2)} = 2\mathbb{Z}$.

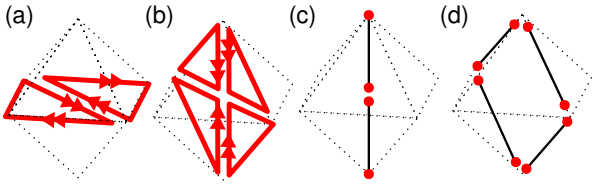

Figure 13. a) Construction of second-order boundary states for a crystal with $\mathcal{M}_z$ and $\mathcal{R}_{2,z}$ symmetries by placing 2D topological superconductors on the two 2-cells in the mirror plane. b) Placing 2D superconductors on the four 2-cells perpendicular to the mirror plane is not allowed, because the copropagating chiral Majorana modes at the interior boundaries between cells can not be gapped out. c) Third-order boundary states with well-defined $\mathcal{R}_{2,z}$ parity can be obtained by placing 1D superconductors at the two 1-cells along the rotation axis. d) Extrinsic third-order boundary states, consisting of pairs of corner states with different $\mathcal{R}_{2,z}$ parity, arise from 1D topological phases at the four boundary 1-cells outside the mirror plane.

To construct third-order boundary states, we place 1D topological superconducting phases on the two 1-cells along the rotation axis (see Figure 13c). Because of the presence of the local $\mathcal{R}_{2,z}$ symmetry commuting with $\mathcal{P}$, such 1D topological superconducting phases have a $\mathbb{Z}_2^2$ classification, because the Majorana end states have well-defined $\mathcal{R}_{2,z}$-parity. Because $\mathcal{M}_z$ commutes with $\mathcal{R}_{2,z}$, the two mirror-related Majorana states at the crystal center have the same $\mathcal{R}_{2,z}$ parity and can mutually gap out. There are no 1D topological superconductors with an onsite symmetry anticommuting with $\mathcal{P}$,[21] so placing topological phases onto the two 1-cells in the mirror plane is not possible. We thus conclude that $\mathcal{K}^{(3)} = \mathbb{Z}_2^2$, corresponding to Majorana corner states on the rotation axis with even or odd $\mathcal{R}_{2,z}$ parity.

To find the decoration group $\mathcal{D}^{(2)}$, we consider 2D topological superconductors placed on the eight faces of $\partial\mathbf{\Omega}_2$ (see Figure 7c). The counterpropagating Majorana modes at the "seams" between boundary 2-cells outside the mirror plane are gapped out, while the pairs of copropagating Majorana modes in the mirror plane remain. We conclude that $\mathcal{D}^{(2)} = 2\mathbb{Z}$ and, therefore, $\mathcal{K}_a^{(2)} = 0$. There is a subtlety here: The surface decoration generating $\mathcal{D}^{(2)}$ also contains a corner state at each of the two $\mathcal{R}_{2,z}$-symmetric corners; see Figure 7c. This can be verified by explicit calculation or, alternatively, from the discussion of this example in Section 3.7, where it is shown that a boundary signature with two copropagating Majorana modes in the mirror plane but without a corner state in the two $\mathcal{R}_{2,z}$-symmetric corners is anomalous. As a consequence, using the decoration from $\mathcal{D}^{(2)}$, the hinge states can be gapped out, although by doing so the corner states appear.

To find $\mathcal{D}^{(3)}$ we add 1D topological superconductors at the four boundary 1-cells outside the mirror plane (see Figure 13d). The pairs of Majorana end states in the mirror plane can mutually gap out because $\mathcal{M}_z$ anticommutes with $\mathcal{P}$. What remains is pairs of Majorana corner modes at the two $\mathcal{R}_{2,z}$-symmetric corners, one of each $\mathcal{R}_{2,z}$ parity. No 1D topological superconductors can be pasted onto the four boundary 1-cells in the mirror plane, because the existence of a local symmetry anticommuting with $\mathcal{P}$ rules out topological phases there. We conclude that $\mathcal{D}^{(3)} = \mathbb{Z}_2$ and, therefore, $\mathcal{K}_a^{(3)} = \mathbb{Z}_2$.

5.2. Bulk Classification

We now use the general method outlined in Section 4.2 to show that from the bulk perspective the odd-parity superconductor with point group $G = C_{2h}$ is classified by the subgroup sequence

$$2\mathbb{Z} \subset \mathbb{Z} \subset \mathbb{Z} \subset \mathbb{Z} \tag{36}$$

This subgroup sequence is consistent with the boundary classification (Equation (35)).

A Dirac Hamiltonian for this class was discussed in Section 3.7. There, the relevant mass terms could easily be found by inspection. To illustrate the systematic formalism of Section 4.2, we here rederive the same results using the Cornfeld–Chapman isomorphism.

We first calculate the full classification group K of 3D gapped Dirac Hamiltonians

$$H = m\Gamma_0 + k_1\Gamma_1 + k_2\Gamma_2 + k_3\Gamma_3 \tag{37}$$

with particle–hole constraint $U_{\mathcal{P}}$ with $\mathcal{P}^2 = 1$, twofold rotation symmetry $U_{\mathcal{R}}$, and mirror symmetry $U_{\mathcal{M}}$. At this point no explicit representation of the gamma matrices and of the symmetry representations $U_{\mathcal{P}}$, $U_{\mathcal{R}}$, and $U_{\mathcal{M}}$ needs to be specified. The Dirac matrices Γ_i provide a representation $U_R^\Gamma = ie^{\Gamma_1\Gamma_2\pi/2}$ of twofold rotation symmetry and a representation $U_{\mathcal{CM}}^\Gamma = \Gamma_3$ of a mirror *antisymmetry*. The superscript Γ denotes that these representations are constructed from the Dirac Hamiltonian and that they in general satisfy different algebraic relations than the point-group symmetries $\mathcal{R}_{2,z}$ and $\mathcal{M}_z$. According to the Cornfeld–Chapman isomorphism, the topological classification of Dirac Hamiltonians with the point group G is the same as the topological classification of Dirac Hamiltonians with the onsite symmetries

$$U_{\mathcal{R}}^{\mathcal{O}} = U_{\mathcal{R}}^\Gamma U_{\mathcal{R}},\ U_{\mathcal{M}}^{\mathcal{C}} = iU_{\mathcal{CM}}^\Gamma U_{\mathcal{M}} \tag{38}$$

Here the superscripts $\mathcal{O}$ and $\mathcal{C}$ indicate that the representation acts as onsite symmetry or antisymmetry (i.e., chiral constraint), respectively.

The local symmetries $\mathcal{O}_{\mathcal{R}}$ and $\mathcal{C}_{\mathcal{M}}$ obtained in this manner have different algebraic relations to $\mathcal{P}$ than the original symmetries $\mathcal{R}$ and $\mathcal{M}$, although they still mutually commute: $\mathcal{O}_{\mathcal{R}}$ anticommutes with $\mathcal{P}$, whereas $\mathcal{C}_{\mathcal{M}}$ commutes with $\mathcal{P}$. By considering a basis with well-defined parity $\pm$ under $\mathcal{O}_{\mathcal{R}}$, the Dirac Hamiltonian is block-diagonalized, $H = \mathrm{diag}(h_+, h_-)$. Because $\mathcal{P}$ anticommutes with $\mathcal{O}_{\mathcal{R}}$, h_+ and h_- are related to each other by $\mathcal{P}$, so it is sufficient to classify the even-parity block h_+. As the only constraint on this block is the antisymmetry $\mathcal{C}_{\mathcal{M}}$, it belongs to the tenfold-way class AIII, which has a $K = \mathbb{Z}$ classification in three spatial dimensions.[5,6] To find the corresponding topological invariant, one has to write h_+ in the Dirac form, similar to Equation (37), with gamma matrices γ_i, $i = 0, 1, 2, 3$, and find the representation $u_{\mathcal{M}}^{\mathcal{C}}$ of the onsite antisymmetry within this block. The topological invariant $\mathcal{N}$ then reads[56]

$$\mathcal{N} = \frac{1}{4}\mathrm{tr}\gamma_0\gamma_1\gamma_2\gamma_3 u_{\mathcal{M}}^{\mathcal{C}} \tag{39}$$

For the calculation of the subgroup $K^{(3)}$ classifying the atomic limit phases, we consider Dirac Hamiltonians with three mass terms M_i, $i = 1, 2, 3$, and the 3D vector representation $O_3^{\mathrm{vec}}(\mathcal{R}_{2,z}) = -O_3^{\mathrm{vec}}(\mathcal{M}_z) = \mathrm{diag}(-1, -1, 1)$ of the point group. The classification group $K_{O_3^{\mathrm{vec}}}$ classifies an extended Dirac Hamiltonian with three "defect coordinates" x, y, and z

$$H_{O_3^{\mathrm{vec}}} = H + xM_1 + yM_2 + zM_3 \tag{40}$$

where H is the Dirac Hamiltonian given in Equation (37). Similarly as before, we construct a representation $\tilde{U}_{\mathcal{R}}^\Gamma = e^{\Gamma_1\Gamma_2\pi/2}e^{M_1M_2\pi/2}$ of twofold rotation symmetry and $\tilde{U}_{\mathcal{M}}^\Gamma = i\Gamma_3M_3$ of mirror *symmetry* using the gamma matrices and mass terms appearing in Equation (40). Applying the Cornfeld–Chapman isomorphism, we map the problem of classifying the defect Hamiltonian (Equation (40)) with the spatially nonlocal symmetry constraints $\mathcal{R}$ and $\mathcal{M}$ to that of the classification with the local symmetry constraints

$$\tilde{U}_{\mathcal{R}}^{\mathcal{O}} = \tilde{U}_{\mathcal{R}}^\Gamma U_{\mathcal{R}},\ \tilde{U}_{\mathcal{M}}^{\mathcal{O}} = \tilde{U}_{\mathcal{M}}^\Gamma U_{\mathcal{M}} \tag{41}$$

In this case, the onsite symmetry $\tilde{\mathcal{O}}_{\mathcal{R}}$ commutes with $\mathcal{P}$, whereas $\tilde{\mathcal{O}}_{\mathcal{M}}$ anticommutes with $\mathcal{P}$. We use a basis with well-defined parity under $\tilde{\mathcal{O}}_{\mathcal{R}}$ to write $H_{O_3^{\mathrm{vec}}}$ in block diagonal form, $H_{O_3^{\mathrm{vec}}} = \mathrm{diag}(h_+, h_-)$. The two blocks $h_\pm$ of even/odd parity states are classified independently. Each of these blocks can again be divided into two subblocks, $h_\pm = \mathrm{diag}(h_{\pm,+}, h_{\pm,-})$, defined according to the parity under $\tilde{\mathcal{O}}_{\mathcal{M}}$. The subblocks $h_{\pm,+}$ and $h_{\pm,-}$ are not independent, as they are mapped onto each other by $\mathcal{P}$. Therefore, only two independent blocks remain, say $h_{\pm,+}$. Each of these is in tenfold-way class A, because no further symmetry constraints apply. As shown by Teo and Kane,[63] the 3D Dirac Hamiltonian with three defect dimensions (Equation (40)) has the same classification as 0D Hamiltonians in tenfold-way class A. Accordingly, we have $K_{O_3^{\mathrm{vec}}} = \mathbb{Z}^2$.

The image of the inclusion $K_{O_3^{\mathrm{vec}}} \mapsto K$ is obtained by calculating the topological invariant (Equation (39)) for the two generators of $K_{O_3^{\mathrm{vec}}}$. At this point, it is helpful to introduce a concrete realization of the Dirac matrices and mass terms of the generator of $K_{O_3^{\mathrm{vec}}}$ with even or odd $\tilde{\mathcal{O}}_{\mathcal{R}}$ parity

$$\begin{aligned}\tilde{\gamma}_0 &= -\mu_3\tau_3\sigma_2\\ (\tilde{\gamma}_1, \tilde{\gamma}_2, \tilde{\gamma}_3) &= -(\tau_3\mu_3\rho_3\sigma_2, \tau_3\mu_3\rho_2, \tau_3\mu_2)\\ (\tilde{m}_1, \tilde{m}_2, \tilde{m}_3) &= (\tau_3\mu_3\rho_3\sigma_1, \tau_3\mu_3\rho_1, \tau_3\mu_1)\end{aligned} \tag{42}$$

with constraints $\tilde{u}_{\mathcal{P}} = \tau_1$, $\tilde{u}_{\mathcal{M}}^{\mathcal{O}} = \tau_3$, and $\tilde{u}_{\mathcal{R}}^{\mathcal{O}} = \pm 1$. To calculate the image in K, we first transform back to the original formulation with spatial symmetries $\mathcal{M}$ and $\mathcal{R}$ using the inverse of Equation (41). This gives $U_{\mathcal{R}} = \pm\rho_3\sigma_3$ and $U_{\mathcal{M}} = \tau_3\mu_3$. Next, we use Equation (38) to transform to the onsite constraints $U_{\mathcal{R}}^{\mathcal{O}} = \pm\rho_2\sigma_1$ and $U_{\mathcal{M}}^{\mathcal{C}} = \mu_1$ and project onto the even-parity block h_+. Calculating the topological invariant (Equation (39)) then gives $\mathcal{N} = \pm 2$. We conclude that the image of $K_{O_3^{\mathrm{vec}}} \mapsto K$ is $K^{(3)} = 2\mathbb{Z}$.

Finally, to calculate $K^{(2)}$ we need to consider all 2D representations of two mass terms that correspond to third-order boundary states for all relevant 2D real representations O_2 of C_{2h}. We here consider the representation $O_2(\mathcal{M}_z) = -O_2(\mathcal{R}_{2,z}) = \mathrm{diag}(1, 1)$. Other representations are possible, too, and can be treated with the same formalism, but do not affect our conclusions. The classifying group K_{O_2} classifies defect Hamiltonians of form

$$H_{O_2} = H + xM_1 + yM_2 \tag{43}$$

where H is the Dirac Hamiltonian of Equation (37). The Cornfeld–Chapman isomorphism maps the point-group symmetries to local symmetry representations

$$\bar{U}_{\mathcal{R}}^{\mathcal{O}} = e^{\Gamma_1\Gamma_2\pi/2}e^{M_1M_2\pi/2}U_{\mathcal{R}},\ \bar{U}_{\mathcal{M}}^{\mathcal{C}} = i\Gamma_3U_{\mathcal{M}} \tag{44}$$

where $\bar{\mathcal{O}}_{\mathcal{R}}$ and $\bar{\mathcal{C}}_{\mathcal{M}}$ commute with $\mathcal{P}$ and mutually. Block-diagonalizing H_{O_2} according to the $\bar{\mathcal{O}}_{\mathcal{R}}$ parity gives two independent blocks $\bar{h}_\pm$, which are effectively in tenfold-way class BDI because of the local constraints $\bar{\mathcal{C}}_{\mathcal{M}}$ and $\mathcal{P}$. The topological classification of 3D Dirac Hamiltonians with two defect coordinates x and y is the same as the classification of 1D Dirac Hamiltonians,[63] which have the classifying group $\mathbb{Z}$ for

class BDI. As the two blocks with even and odd $\mathcal{O}_{\mathcal{R}}$ parity are independent, we arrive at the classifying group $K_{O_2} = \mathbb{Z}^2$.

To find the image of the inclusion $K_{O_2} \mapsto K$, we start from an explicit realization of the two generators of a 3D Dirac Hamiltonian in class BDI with defect dimension two

$$\begin{aligned} \bar{\gamma}_0 &= \mu_3\tau_3\sigma_2 \\ (\bar{\gamma}_1, \bar{\gamma}_2, \bar{\gamma}_3) &= (\mu_3\tau_3\sigma_1, \mu_3\tau_3\sigma_3, \mu_3\tau_1) \\ (\bar{m}_1, \bar{m}_2) &= (\mu_3\tau_2, \mu_2) \end{aligned} \tag{45}$$

with constraints $\bar{u}_{\mathcal{P}} = 1$, $\bar{u}_{\mathcal{C}} = \mu_1$, and $\bar{u}^{\mathcal{O}}_{\mathcal{R}} = \pm 1$. As before, we first map back to the formulation with the spatial symmetries $U_{\mathcal{M}}$ and $U_{\mathcal{R}}$ using the inverse of Equation (44), which gives $U_{\mathcal{R}} = \pm\mu_1\tau_2\sigma_2$ and $U_{\mathcal{M}} = \mu_2\tau_1$, and then map to a formulation with the onsite constraints $U^{\mathcal{O}}_{\mathcal{R}} = \pm\mu_1\tau_2$ and $U^{\mathcal{C}}_{\mathcal{M}} = \mu_1$ using Equation (38). Finally, we transform to a basis with well-defined $U^{\mathcal{O}}_{\mathcal{R}}$-parity and find the topological invariants $\mathcal{N} = \pm 1$. From this, we conclude that $K^{(2)} = \mathbb{Z}$.

6. Conclusion

The discovery of higher-order topological phases[13] provided important insights for the classification of topological crystalline insulators and superconductors. In one set of classification approaches,[19,26,54,61] one first classifies anomalous higher-order boundaries and symmetry-obstructed atomic limits, and then, assuming bulk–boundary correspondence, finds the bulk classification group K. A different classification paradigm uses algebraic methods to classify Dirac Hamiltonians.[9–11,43] Both approaches provide complete classifications and a set of generating models; the latter approach provides minimal Dirac models, whereas the former one uses the "topological crystalline construction,"[61] which typically results in models with a nonminimal unit cell.

The quest for novel topological materials requires not only the knowledge of topological classification, but also an efficient method to relate the given band structure to its boundary signatures. One possibility in this regard is an algorithm that "deforms" a given band structure to a form that is close to a Dirac-like phase transition. The other possibility, which is actively pursued by many research groups, concerns the construction of easy-to-compute topological invariants. If, furthermore, such topological invariants are designed to "detect" only band structures with anomalous boundary states, one refers to these as symmetry-based indicators.[34,35,64] Symmetry-based indicators were initially constructed for insulators, and have been recently extended to superconductors.[57,65–70] Although symmetry-based indicators in general do not provide a full classification, their construction and subsequent application resulted in the discovery of many new topological insulator materials[71,72]. It remains to be seen if the same will be the case for topological superconductors.

Acknowledgements

The authors thank Max Geier, Titus Neupert, and Felix von Oppen for discussions. L.T. thanks Ken Shiozaki for useful discussions about the Cornfeld–Chapman isomorphism. The authors acknowledge support by project A03 of the CRC-TR 183 and by the priority programme SPP 1666 of the German Science Foundation DFG (PWB), as well as by the Ambizione Grant PZ00P2.179962 of the FNS/SNF (LT).

Conflict of Interest

The authors declare no conflict of interest.

Keywords

higher-order topological phases, topological crystalline insulators and superconductors, topology

Received: February 17, 2020
Revised: July 3, 2020
Published online: August 31, 2020

[1] B. A. Bernevig, T. L. Hughes, *Topological Insulators and Topological Superconductors*, Princeton University Press, Princeton, NJ **2013**.
[2] Y. Ando, L. Fu, *Annu. Rev. Condens. Matter Phys.* **2015**, *6*, 361.
[3] M. Z. Hasan, C. L. Kane, *Rev. Mod. Phys.* **2010**, *82*, 3045.
[4] X. L. Qi, S. C. Zhang, *Rev. Mod. Phys.* **2011**, *83*, 1057.
[5] A. Kitaev, *AIP Conf. Proc.* **2009**, *1134*, 22.
[6] A. P. Schnyder, S. Ryu, A. Furusaki, A. W. W. Ludwig, *AIP Conf. Proc.* **2009**, *1134*, 10.
[7] A. M. Turner, Y. Zhang, R. S. K. Mong, A. Vishwanath, *Phys. Rev. B* **2012**, *85*, 165120.
[8] L. Fu, *Phys. Rev. Lett.* **2011**, *106*, 106802.
[9] C. K. Chiu, H. Yao, S. Ryu, *Phys. Rev. B* **2013**, *88*, 075142.
[10] T. Morimoto, A. Furusaki, *Phys. Rev. B* **2013**, *88*, 125129.
[11] K. Shiozaki, M. Sato, *Phys. Rev. B* **2014**, *90*, 165114.
[12] L. Trifunovic, P. W. Brouwer, *Phys. Rev. B* **2017**, *96*, 195109.
[13] F. Schindler, A. M. Cook, M. G. Vergniory, Z. Wang, S. S. P. Parkin, B. A. Bernevig, T. Neupert, *Sci. Adv.* **2018**, *4*, eaat0346.
[14] W. A. Benalcazar, B. A. Bernevig, T. L. Hughes, *Phys. Rev. B* **2017**, *96*, 245115.
[15] J. Langbehn, Y. Peng, L. Trifunovic, F. von Oppen, P. W. Brouwer, *Phys. Rev. Lett.* **2017**, *119*, 246401.
[16] Z. Song, Z. Fang, C. Fang, *Phys. Rev. Lett.* **2017**, *119*, 246402.
[17] C. Fang, L. Fu, *Sci. Adv.* **2019**, *5*, eaat2374.
[18] M. Geier, L. Trifunovic, M. Hoskam, P. W. Brouwer, *Phys. Rev. B* **2018**, *97*, 205135.
[19] E. Khalaf, H. C. Po, A. Vishwanath, H. Watanabe, *Phys. Rev. X* **2018**, *8*, 031070.
[20] E. Khalaf, *Phys. Rev. B* **2018**, *97*, 205136.
[21] L. Trifunovic, P. W. Brouwer, *Phys. Rev. X* **2019**, *9*, 011012.
[22] J. Ahn, S. Park, D. Kim, Y. Kim, B. J. Yang, *Chin. Phys. B* **2019**, *28*, 117101.
[23] N. Okuma, M. Sato, K. Shiozaki, *Phys. Rev. B* **2019**, *99*, 085127.
[24] E. Roberts, J. Behrends, B. Béri, *Phys. Rev. B* **2020**, *101*, 155133.
[25] S. H. Kooi, G. van Miert, C. Ortix, *Phys. Rev. B* **2019**, *100*, 115160.
[26] A. Rasmussen, Y. M. Lu, *Phys. Rev. B* **2020**, *101*, 085137.
[27] G. E. Volovik, *JETP Lett.* **2010**, *91*, 201.
[28] M. Sitte, A. Rosch, E. Altman, L. Fritz, *Phys. Rev. Lett.* **2012**, *108*, 126807.
[29] F. Zhang, C. L. Kane, E. J. Mele, *Phys. Rev. Lett.* **2013**, *110*, 046404.
[30] D. J. Thouless, M. Kohmoto, M. P. Nightingale, M. den Nijs, *Phys. Rev. Lett.* **1982**, *49*, 405.
[31] W. P. Su, J. R. Schrieffer, A. J. Heeger, *Phys. Rev. Lett.* **1979**, *42*, 1698.
[32] A. Y. Kitaev, *Phys. Usp.* **2001**, *44*, 131.

[33] A. Lau, J. van den Brink, C. Ortix, *Phys. Rev. B* **2016**, *94*, 165164.
[34] H. C. Po, A. Vishwanath, H. Watanabe, *Nat. Commun.* **2017**, *8*, 50.
[35] B. Bradlyn, L. Elcoro, J. Cano, M. G. Vergniory, Z. Wang, C. Felser, M. I. Aroyo, B. A. Bernevig, *Nature* **2017**, *547*, 298.
[36] C. K. Chiu, J. C. Y. Teo, A. P. Schnyder, S. Ryu, *Rev. Mod. Phys.* **2016**, *88*, 035005.
[37] W. A. Benalcazar, B. A. Bernevig, T. L. Hughes, *Science* **2017**, *357*, 61.
[38] G. van Miert, C. Ortix, *Phys. Rev. B* **2018**, *98*, 081110.
[39] S. Ono, L. Trifunovic, H. Watanabe, *Phys. Rev. B* **2019**, *100*, 245133.
[40] W. A. Benalcazar, T. Li, T. L. Hughes, *Phys. Rev. B* **2019**, *99*, 245151.
[41] J. C. Y. Teo, T. L. Hughes, *Phys. Rev. Lett.* **2013**, *111*, 047006.
[42] W. A. Benalcazar, J. C. Y. Teo, T. L. Hughes, *Phys. Rev. B* **2014**, *89*, 224503.
[43] E. Cornfeld, A. Chapman, *Phys. Rev. B* **2019**, *99*, 075105.
[44] S. Imhof, C. Berger, F. Bayer, J. Brehm, L. W. Molenkamp, T. Kiessling, F. Schindler, C. H. Lee, M. Greiter, T. Neupert, R. Thomale, *Nat. Phys.* **2018**, *14*, 925.
[45] M. Serra-Garcia, R. Süsstrunk, S. D. Huber, *Phys. Rev. B* **2019**, *99*, 020304.
[46] C. W. Peterson, W. A. Benalcazar, T. L. Hughes, G. Bahl, *Nature* **2018**, *555*, 346.
[47] M. Serra-Garcia, V. Peri, R. Süsstrunk, O. R. Bilal, T. Larsen, L. G. Villanueva, S. D. Huber, *Nature* **2018**, *555*, 342.
[48] S. N. Kempkes, M. R. Slot, J. J. van den Broeke, P. Capiod, W. A. Benalcazar, D. Vanmaekelbergh, D. Bercioux, I. Swart, C. Morais Smith, *Nat. Mater.* **2019**, *18*, 1292.
[49] F. Schindler, Z. Wang, M. G. Vergniory, A. M. Cook, A. Murani, S. Sengupta, A. Y. Kasumov, R. Deblock, S. Jeon, I. Drozdov, H. Bouchiat, S. Guéron, A. Yazdani, B. A. Bernevig, T. Neupert, *Nat. Phys.* **2018**, *14*, 918.
[50] A. K. Nayak, J. Reiner, R. Queiroz, H. Fu, C. Shekhar, B. Yan, C. Felser, N. Avraham, H. Beidenkopf, *Sci. Adv.* **2019**, *5*, eaax6996.
[51] R. Noguchi, M. Kobayashi, Z. Jiang, K. Kuroda, T. Takahashi, Z. Xu, D. Lee, M. Hirayama, M. Ochi, T. Shirasawa, P. Zhang, C. Lin, C. Bareille, S. Sakuragi, H. Tanaka, S. Kunisada, K. Kurokawa, K. Yaji, A. Harasawa, V. Kandyba, A. Giampietri, A. Barinov, T. K. Kim, C. Cacho, M. Hashimoto, D. Lu, S. Shin, R. Arita, K. Lai, T. Sasagawa, T. Kondo, arXiv:2002.01134, **2020**.
[52] A. Murani, A. Kasumov, S. Sengupta, Y. A. Kasumov, V. T. Volkov, I. I. Khodos, F. Brisset, R. Delagrange, A. Chepelianskii, R. Deblock, H. Bouchiat, S. Guéron, *Nat. Commun.* **2017**, *8*, 15941.
[53] I. C. Fulga, F. Hassler, A. R. Akhmerov, C. W. J. Beenakker, *Phys. Rev. B* **2011**, *83*, 155429.
[54] K. Shiozaki, C. Zhaoxi Xiong, K. Gomi, arXiv:1810.00801, **2018**.
[55] R. Thorngren, D. V. Else, *Phys. Rev. X* **2018**, *8*, 011040.
[56] K. Shiozaki, arXiv:1907.09354, **2019**.
[57] M. Geier, P. W. Brouwer, L. Trifunovic, *Phys. Rev. B* **2020**, *101*, 245128.
[58] T. I. Tuegel, V. Chua, T. L. Hughes, *Phys. Rev. B* **2019**, *100*, 115126.
[59] H. Isobe, L. Fu, *Phys. Rev. B* **2015**, *92*, 081304.
[60] I. C. Fulga, N. Avraham, H. Beidenkopf, A. Stern, *Phys. Rev. B* **2016**, *94*, 125405.
[61] S. J. Huang, H. Song, Y. P. Huang, M. Hermele, *Phys. Rev. B* **2017**, *96*, 205106.
[62] Z. D. Song, L. Elcoro, B. A. Bernevig, *Science* **2019**, *367*, 794.
[63] J. C. Y. Teo, C. L. Kane, *Phys. Rev. B* **2010**, *82*, 115120.
[64] J. Kruthoff, J. de Boer, J. van Wezel, C. L. Kane, R. J. Slager, *Phys. Rev. X* **2017**, *7*, 041069.
[65] S. Ono, H. Watanabe, *Phys. Rev. B* **2018**, *98*, 115150.
[66] S. Ono, Y. Yanase, H. Watanabe, *Phys. Rev. Res.* **2019**, *1*, 013012.
[67] S. Ono, H. C. Po, H. Watanabe, *Sci. Adv.* **2019**, *6*, eaaz8367.
[68] K. Shiozaki, arXiv:1907.13632, **2019**.
[69] A. Skurativska, T. Neupert, M. H. Fischer, *Phys. Rev. Res.* **2020**, *2*, 013064.
[70] F. Schindler, B. Bradlyn, M. H. Fischer, T. Neupert, *Phys. Rev. Lett.* **2020**, *124*, 247001.
[71] T. Zhang, Y. Jiang, Z. Song, H. Huang, Y. He, Z. Fang, H. Weng, C. Fang, *Nature* **2019**, *566*, 475.
[72] M. G. Vergniory, L. Elcoro, C. Felser, N. Regnault, B. A. Bernevig, Z. Wang, *Nature* **2019**, *566*, 480.

Luka Trifunovic studied physics at the University of Belgrade in Serbia. After obtaining his Ph.D. from the University of Basel in 2014, two postdoctoral stays at Freie Universität Berlin (Germany) and RIKEN (Japan) followed. He is currently an Ambizione fellow at the University of Zürich (Switzerland).

Piet Brouwer studied physics and mathematics at Leiden University (The Netherlands). After a postdoctoral stay at Harvard University, he took up a faculty position at Cornell University (USA). In 2009, following the award of an Alexander von Humboldt Professorship, he became a professor at Freie Universität Berlin.